



國立臺灣大學理學院大氣科學研究所

碩士論文

Graduate Institute of Atmospheric Sciences

College of Science

National Taiwan University

Master's Thesis

2019 年利奇馬颱風之長生命期雙眼牆結構維持機制：

軸對稱觀點

Maintenance Mechanisms of the Long-Lived Concentric

Eyewall Structure of Typhoon Lekima (2019):

Axisymmetric Perspective

李尚恩

Shang-En Li

指導教授：楊明仁 博士

Advisor: Ming-Jen Yang Ph.D.

中華民國 113 年 1 月

January 2024



國立臺灣大學碩士學位論文 口試委員會審定書

本論文係 李尚恩 君 (學號 R08229009) 在國立臺灣大學大氣科學學系、所完成之碩士學位論文，於民國 112 年 12 月 25 日承下列考試委員審查通過及口試及格，特此證明

口試委員：

楊明仁 (簽名)
(指導教授)

郭鴻基
黃靖勇

陳正平

系主任、所長

游政宏 (簽名)

誌謝



經過四年半的研究所生涯，終於走到即將離開學校的這一步。這一路以來研究的完成與經歷的難關，必須感謝身邊的家人、師長、朋友的幫助，碩士論文才得以完成。感謝我的指導老師，楊明仁老師，在研究的路上一步步引導我，讓我知道研究方向應如何進展，也讓我學習到做研究時應有的想法與態度；感謝老師給我這個舞台，讓我在研究中盡情享受撰寫程式的樂趣，及給予我充足的時間讓我得以維護研究程式的品質。感謝對研究非常熱血的郭鴻基老師，給予我研究上諸多建議與啟發。感謝口試委員郭鴻基老師、陳正平老師、黃清勇老師給予論文建議，這篇碩士論文得以更加完整。感謝國立臺灣大學與電腦課程開設老師，滿足我對程式的好奇心，使我能運用平行計算提高研究效率。

感謝對流與降水實驗室的夥伴們，也給予我許多研究上的幫助。感謝曜竹給予我 WRF 模式的技術指導，感謝炯恩給予我研究道路上的經驗分享，感謝茂正給予我人生道路上的指點、感謝世暘、若瑜、詣軒給予我歡樂、感謝九令的讀書會讓我有舞台展現我的程式技術。

儘管研究所生涯經歷人生低潮，感謝楊老師在我狀況不好的時候給我充足的時間休息，感謝郭老師對我的關心，感謝曜竹與炯恩對我的關懷，感謝禹安、秉恩、毓琇、峻愷陪我吃飯聊天、感謝奕翰陪我打羽球。感謝你們的陪伴讓我在低潮中過得不孤獨。感謝其他朋友在我的研究所生涯中給予歡樂與陪伴。

研究所生涯很長，感謝家人時時刻刻支持，並在我下重要決定前給予我更完整的評估與觀點，並讓我能無後顧之憂的專心做研究。

最後，感謝自己在這四年半的研究生涯中，遇到困境都能勇敢面對，技術問題都能一一解決，研究的各種關卡都一一挺過。感謝自己在低潮期維持正常的生活作息，研究才能持續完成。

摘要

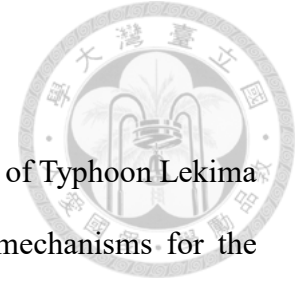


本論文從軸對稱的觀點探討 2019 年利奇馬颱風的長生命期雙眼牆結構。本論文使用網格大小細至 1 公里的高解析 WRF 模式模擬利奇馬颱風，探討可能的雙眼牆維持機制。藉由解 Sawyer-Eliassen 方程式，可診斷出對應潛熱加熱分布所反映的次環流(徑向風、垂直速度)結構；將位於內眼牆、外眼牆、兩眼牆間的 moat 區域的潛熱加熱分別代入 Sawyer-Eliassen 方程式，就可診斷出對應區域潛熱加熱所貢獻的 moat 區下沉氣流。藉由計算 dynamic efficiency factor (DEF)，水氣被外眼牆限制的內眼牆處，潛熱加熱轉換至切向風的能量轉換效率也可被診斷。

Sawyer-Eliassen 診斷結果顯示，雙眼牆形成後，moat 區的下沉氣流主要由內眼牆及外眼牆的潛熱加熱貢獻，由 moat 區的潛熱冷卻為次要貢獻。DEF 診斷結果顯示，內眼牆處的潛熱加熱轉換至切向風的轉換效率較外眼牆處大。雖然邊界層內切向風因摩擦力而減弱，內眼牆補償的切向風較外眼牆補償的切向風大，抵銷一部分摩擦減弱的切向風。補償的切向風可以在 moat 區海洋表層吸收更多水氣，增加內眼牆的水氣供應，增加潛熱轉換至動能的總能量。雖然利奇馬颱風內眼牆最後受外眼牆的水氣阻斷而減弱，內眼牆仍可因潛熱加熱的高 DEF 而維持數十小時。

關鍵詞：熱帶氣旋、雙眼牆、軸對稱動力、Sawyer-Eliassen 方程式、dynamic efficiency factor。

Abstract

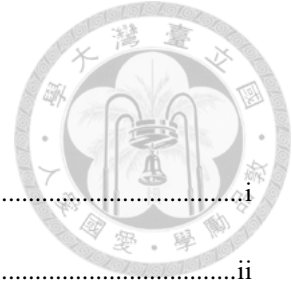


This study examines the long-lived concentric eyewall structure of Typhoon Lekima (2019) from an axisymmetric perspective. Possible maintenance mechanisms for the concentric eyewalls are investigated using a high-resolution WRF simulation (nested down to 1-km horizontal grid size). The secondary-circulation responses to the latent heating in the inner eyewall, moat and outer eyewall are diagnosed by solving the Sawyer-Eliassen equation individually to examine the corresponding contribution to the moat downdraft. By calculating the dynamic efficiency factor (DEF), the conversion of latent heating to kinetic energy is evaluated in the moisture-restricted inner eyewall.

The Sawyer-Eliassen diagnoses show that the moat downdraft was contributed mainly by latent heating in the inner and outer eyewall, with a secondary contribution from latent cooling in the moat after concentric eyewall formation. DEF diagnoses show that the conversion of latent heating to kinetic energy in the inner eyewall was more efficient than in the outer eyewall. Although tangential wind within the boundary layer was weakened by friction, the compensative tangential wind in the inner eyewall was larger than in the outer eyewall. The compensative tangential wind indirectly accumulated moisture from the sea surface in the moat, aiding the moisture supply to the inner eyewall and enhancing the amount of kinetic energy converted from latent heating. Although the inner eyewall of Typhoon Lekima eventually weakens due to the moisture cut off from the outer eyewall, the inner eyewall can still be maintained for tens of hours by the high DEF from latent heating.

Keywords: Tropical cyclone; concentric eyewall; axis symmetry; Sawyer-Eliassen equation; dynamic efficiency factor

Table of Contents



| | |
|--|------|
| 國立臺灣大學碩士學位論文口試委員審定書 | i |
| 誌謝 | ii |
| 摘要 | iii |
| Abstract | iv |
| Table of Contents | v |
| List of Tables | vii |
| List of Figures | viii |
| Chapter 1. Introduction | 1 |
| Chapter 2. Methodology | 8 |
| 2.1 WRF configuration | 8 |
| 2.2 Sawyer-Eliassen diagnoses | 9 |
| 2.3 Dynamic efficiency factor diagnoses | 13 |
| Chapter 3. Case Overview | 16 |
| 3.1 Observations | 16 |
| 3.2 Model results | 17 |
| 3.3 Axisymmetry | 20 |
| Chapter 4. Diagnosis Results | 22 |
| 4.1 Results of Sawyer-Eliassen diagnoses | 22 |
| 4.2 Results of dynamic efficiency factor diagnoses | 28 |
| Chapter 5. Conclusions and future work | 35 |
| 5.1 Conclusions | 35 |
| 5.2 Future work | 39 |
| Acknowledgments | 41 |

| | |
|--------------------|----|
| Open Research..... | 41 |
| Reference..... | 43 |
| Tables | 50 |
| Figures..... | 51 |



List of Tables

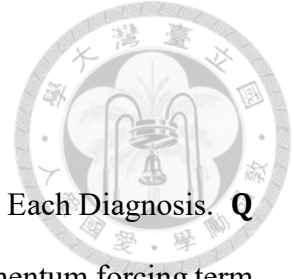


Table 1. Ranges of Forcing Terms for the Sawyer-Eliassen Equation in Each Diagnosis. **Q** is the diabatic heating rate including latent heating, and **F** is the momentum forcing term from PBL Scheme..... 50

List of Figures



Figure 1: The nested domain of the WRF model and the track of TC Lekima from 0000 UTC 5 August to 11 August 2019. Note that both the 3-km and 1-km domains are moving with the TC, with the center of the 1-km domain located at the eye of TC Lekima. 51

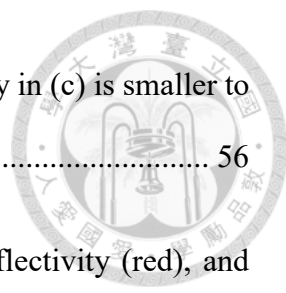
Figure 2: The (a) tracks, (b) sea-level pressure (hPa), and (c) 10-m height wind speed (kt) of TC Lekima from the JMA best-track data (in orange) and the WRF simulation (in blue). The dots are marked every 6 hours. The black dots marked with numbers along the track in (a) indicate the positions of TC Lekima at 0000 UTC that day..... 52

Figure 3: The 0.2° elevation angle PPI reflectivity (colored; dBZ) from the radar on Ishigaki Island at (a) 0605 UTC and (b) 1805 UTC 8 August 2019, and the 0.5° elevation angle PPI reflectivity (dBZ) from the radar on Wufen Mountain at (c) 0302 UTC and (d) 1602 UTC on 9 August 2019..... 53

Figure 4: Hovmöller diagram of 2-km azimuthally-averaged reflectivity (colored: dBZ) observed by Ishigaki Island radar. 54

Figure 5: Simulated reflectivity (colored; dBZ) at the height of 2 km from 06 UTC on 8 August 2019 to 06 UTC on 9 August 2019 with an interval of 3 hours. The black circles indicate the distances from the TC center with an interval of 40 km. The arrow indicated the vertical wind shear direction between 200 and 850 hPa averaged from $r = 200$ km to $r = 800$ km. Numbers on the upper left of each panel indicate the date and hour (UTC). 55

Figure 6: Hovmöller diagram of the simulated azimuthally-averaged (a) reflectivity (colored; dBZ), (b) tangential wind (colored; $m s^{-1}$), and (c) vertical velocity (colored; m



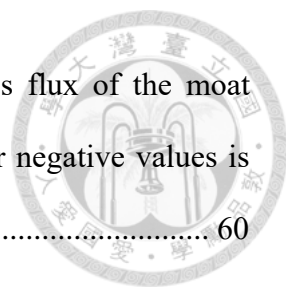
s⁻¹) at z = 2 km. Note that the color scale for negative vertical velocity in (c) is smaller to clarify the moat downdraft. 56

Figure 7: Axisymmetricity parameter of tangential wind (blue), reflectivity (red), and potential vorticity (black) from 7 to 9 August 2019. The orange shading indicates the diagnosed period. The red line indicates the secondary eyewall formation time. 57

Figure 8: (a) Azimuthally-averaged simulated vertical velocity (colored; m s⁻¹); (b), (d), (e), and (f) the corresponding latent heating (colored; K s⁻¹) in Diag2, Diag4, Diag5, Diag6, respectively; and (c), (g), (h), (i) the corresponding momentum forcing (colored; m s⁻²) term in Diag3, Diag7, Diag8, and Diag9, respectively, at 1300 UTC on 8 August 2019. The black lines indicate the outer boundary of the inner eyewall, inner boundary of the outer eyewall, and outer boundary of the outer eyewall. Note that the color scale for negative values is smaller to clarify the moat downdraft and latent cooling rate. Text at the upper-left corner in (b) to (i) indicates the diagnosis experiment. 58

Figure 9: Diagnosed (a) vertical velocity (colored; m s⁻¹) and (b) radial wind (colored; m s⁻¹) by the Sawyer-Eliassen equation. Azimuthally-averaged (c) vertical velocity and (d) radial wind by the WRF simulation. Difference between diagnosed and simulated (e) vertical velocity and (f) radial wind (diagnoses – simulated). Correlation coefficients of (g) vertical velocity and (h) radial wind between the diagnosis and the simulation. Results are at 1300 UTC on 8 August 2019. 59

Figure 10: Diagnosed vertical velocity (colored; m s⁻¹) by considering (a) the latent heating and momentum forcing in the entire domain at 1300 UTC on 8 August 2019. (b-i) Diagnosed vertical velocity by considering the corresponding forcing terms in Figs. 8b to 8i. The black lines in each panel indicate the range of moat downdraft in (b). Text at



the upper side of the panel (a), (b), and (d)-(f) indicates the mass flux of the moat downdraft and the mass flux ratio to that in (b). The color scale for negative values is smaller to clarify the moat downdraft and latent cooling rate. 60

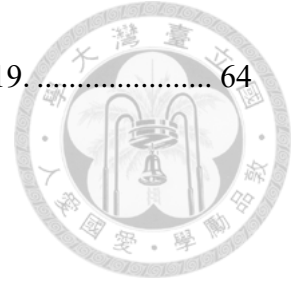
Figure 11: (a) Time series of mass flux of the diagnosed moat downdraft in Diag4 (blue line; kg m s^{-1}), Diag5 (orange line; kg m s^{-1}), and Diag6 (green line; kg m s^{-1}) from 0600 UTC 8 August 2019 to 0600 UTC 9 August 2019 with the 5-min interval. (b) Time series of latent heating in the inner eyewall (solid black line; J s^{-1}), 10 times of latent cooling in the moat (dashed black line; J s^{-1}), 0.1 times of latent heating in the outer eyewall (dotted black line; J s^{-1}), and the simulated moat downdraft mass flux (blue line; kg m s^{-1}). 61

Figure 12: (a) Diagnosed DEF of latent heating (colored; %), (b) diagnosed DEF of momentum (colored; %), (c) simulated azimuthal-averaged baroclinicity (colored; s^{-2}) at 1300 UTC 8 August 2019. The black lines indicate the locations of the radius of maximum wind (RMW) at each altitude, and the cyan lines in (a) and (b) indicate the azimuthally-averaged vertical velocity of 0.05 ms^{-1} 62

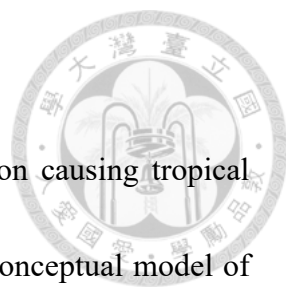
Figure 13: (a) Conversion rate by latent heating at each grid point (colored; $\text{kg m}^{-1} \text{ s}^{-3}$) and (b) conversion rate by momentum forcing at each point (colored; $\text{kg m}^{-1} \text{ s}^{-3}$) at 1300 UTC on 8 August 2019. (c) conversion rate by latent heating (**CH**; blue line; $\text{kg m}^2 \text{ s}^{-2}$) and 10 times conversion rate by momentum forcing (**CM**; blue line; $\text{kg m}^2 \text{ s}^{-2}$) from 1100 UTC to 1700 UTC on 8 August 2019. Cyan and black lines in (a) and (b) indicate the azimuthally-averaged vertical velocity of 0.05 m s^{-1} and the radius of maximum wind (RMW), respectively. 63

Figure 14: (a) Time series of system DEF of latent heating for **$\eta H40$** (orange line; %) and **$\eta H150$** (blue line; %) as well as (b) time series of system DEF of momentum for

$\eta M40$ and **$\eta M150$** from 1100 UTC to 1700 UTC on 8 August 2019..... 64

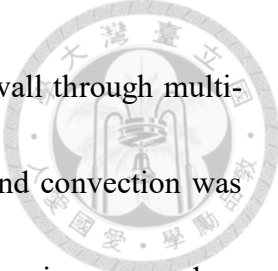


Chapter 1. Introduction



The eyewall replacement cycle (ERC) is a crucial phenomenon causing tropical cyclone (TC) intensity oscillation in hours or tens of hours. In the conceptual model of Willoughby et al. (1982), the outer eyewall first constructs outside the inner eyewall to form concentric eyewalls. Then, the inner eyewall dissipates when the outer eyewall contracts inward, and the TC intensity weakens. Finally, the outer eyewall replaces the inner eyewall after the inner eyewall dissipates completely; the TC intensifies again, and the tangential wind field also widens. The ERC is a common feature in a strong TC with a large maximum wind speed. Kossin and Sitkowski (2009) indicated that about 30 (15) % of category 4 (maximum wind speed $> 58 \text{ ms}^{-1}$) and 60 (50) % of category 5 (maximum wind speed $> 70 \text{ m s}^{-1}$) TCs in the North Atlantic (central and eastern North Pacific) had concentric eyewalls between 1997 to 2006. Kuo et al. (2009) also indicated that about 59% of category 4 and 72% of category 5 TCs in the western North Pacific had concentric eyewalls.

The processes of forming outer eyewall from rainbands have been studied extensively by observation analyses and numerical simulations. For example, Guimond et al. (2020) examined the rainbands associated with the outward-propagated vortex Rossby waves (VRWs) in the aircraft observations of Hurricane Matthew (2016). The VRWs propagated outward, stopped at 3 times the radius of maximum wind (RMW), and



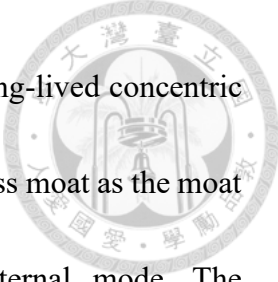
then prolonged the rainband azimuthally to form the secondary eyewall through multi-scale interactions. Wang and Tan (2020) found that the outer-rainband convection was more active if the relative humidity outside the inner core increased, forming a secondary eyewall. Yu et al. (2021) indicated that the mesoscale descending inflow at the rainband can trigger new convective updrafts downwind, which could axisymmetrize the rainband and cause secondary eyewall formation.

When the outer eyewall becomes stronger and more organized, the cutoff effect (i.e., moisture being intercepted by the outer eyewall instead of going to the inner eyewall) will be more evident. It can dissipate the inner eyewall in just a few hours due to insufficient moisture supply. Additionally, inside the outer eyewall is a downdraft, weak reflectivity, and low relative humidity region in the moat with similar dynamics as the eye (Houze et al., 2007; see their Fig. 2); the downdraft is not favorable to the inner-eyewall convection. However, many observations showed that the inner eyewall could survive for tens of hours after the outer eyewall formed in some TCs. Yang et al. (2013) indicated that 23% of TCs in the western North Pacific from 1997 to 2011 had concentric eyewalls, which sustained over 20 hours with a mean duration of 31 hours. This duration is far longer than the mean concentric eyewall duration (16 hours; Yang et al., 2021). These TCs are the most destructive in TCs with concentric eyewalls. The maximum wind speed in long-lived concentric eyewall TCs is 5 m s^{-1} , larger than in other TCs with concentric eyewalls.

The strong intensity can also be sustained longer (Yang et al., 2013). Despite the extensive studies on ERCs, the key roles determining the duration of the ERC are still not well understood.




Concentric eyewall maintenance mechanisms focusing on moat have been much discussed in the literature. Filamentation time measures how strong the horizontal wind shear and deformation to the convection. The filamentation time is short in the moat, highlighting the large deformation and entrainment (Rozoff et al., 2006; Qin et al., 2021). Kuo et al. (2012) examine the convection and rapid filamentation in Typhoon Sinlaku (2008) using the Naval Research Laboratory (NRL) P-3 aircraft data collected during the Tropical Cyclone Structure 2008 (TCS-08) and The Observing System Research and Predictability Experiment (THORPEX) Pacific Asian Regional Campaign (T-PARC) field experiments. Their results indicate that the filamentation process suppresses deep convection in that the ratio of the deep convective region occurrence over the stratiform region varies from around 50% (200%) for filamentation time shorter (longer) than 24 min. The convection-unfavorable moat region isolates the inner eyewall convection from the outer eyewall convection and may affect the concentric eyewall duration. In the long-lived concentric eyewall TCs (i.e., concentric eyewalls maintained for over 20 hours), the moat and outer eyewall widths were 50% larger on average than those in short-lived concentric eyewall TCs (Yang et al., 2013). One possible reason is that the outer eyewall




needs more time to contract due to the broader moat region in the long-lived concentric eyewall TCs (Yang et al., 2013). Kuo et al. (2022) define dimensionless moat as the moat size divided by the Rossby radius of deformation of first internal mode. The dimensionless moat combines the effect of the moat size and the vortex pressure gradient force to accelerate the unbalanced radial inflow and enlarge the inner boundary layer eyewall pumping for inner eyewall convection maintenance. Because the outer eyewall may have some asymmetry, the boundary layer inflow may penetrate the outer eyewall at large azimuthal angles over the region where the convection is weak, and hence sustaining the inner eyewall (Tsujino et al., 2017).

Regardless of an incomplete cutoff effect of the outer eyewall or the reacceleration of the moat inflow, the moisture supply to the inner eyewall in a TC with concentric eyewalls is certainly less than that without the existence of the outer eyewall. The efficiency of converting latent heating to tangential wind speed is vital to maintaining the inner eyewall convection and tangential wind under a moisture-restricted condition. The dynamic efficiency factor (DEF) is a ratio of converting latent heating or momentum forcing to kinetic energy. Kuo et al. (2019) used the diagnoses of DEF of latent heating to investigate the rapid intensification (RI) of TC Haiyan (2013). They found that the DEF of latent heating increased by 33% after the RI onset. Suppose the inner eyewall wind speed can be maintained in insufficient moisture conditions for the long-lived concentric



eyewall TC. In that case, the DEF of latent heating may be larger in the inner eyewall than outside the inner eyewall. The DEF of momentum may also play certain roles in inner eyewall maintenance. It is worth investigating the concentric eyewall maintenance from the DEF perspective.

Long-lived concentric eyewall TCs also have long-lived moats. The moat downdraft keeps the moat in a convection-unfavorable condition to isolate the inner eyewall from the outer eyewall. Finding the formation mechanisms of the moat downdraft is also important to understand concentric eyewall maintenance. Qin et al. (2021) indicated that the downdraft had developed at the location of the future moat before the outer eyewall formed. They argued that the following mechanisms established the original downdraft during the secondary eyewall formation stage. First, the upper-level downdraft was mainly contributed by the compensative downdraft induced by the inner eyewall updraft. That flow brought the low equivalent potential temperature from the environment into the future moat. Then, the latent cooling effect, including evaporation, melting, and sublimation drove the low- and mid-level downdrafts. After the outer eyewall forms, the composition of the moat downdraft likely has been changed. However, the composition of the moat downdraft during the concentric eyewall maintenance has yet to be examined. The Sawyer-Eliassen equation (Eliassen, 1959, 1962; Sawyer, 1956) can diagnose the secondary circulation with a given diabatic heating and/or momentum forcing in a

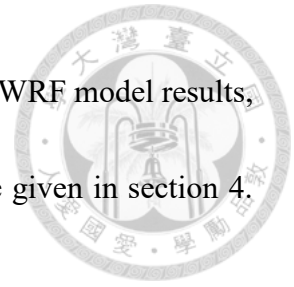


balanced axisymmetric framework. We can individually decompose the latent heating and/or momentum forcing in the inner eyewall, moat, and outer eyewall and then diagnose the corresponding secondary circulation in each region by the given forcing.

Typhoon Lekima (2019) was a TC with long-lived concentric eyewalls. It was observed by the radars on Mt. Wufen (RCWF) and Ishigaki Island and presented concentric eyewalls for almost the entire period within the radar detection range. Before TC Lekima made landfall in China, the concentric eyewalls were maintained for approximately 34 hours, which is far longer than the mean concentric eyewall duration (Yang et al., 2021). This study tries to answer the following scientific questions: 1) While the concentric eyewalls were maintained, what was the contribution from the latent heating in the inner eyewall, moat, and outer eyewall to maintain the moat downdraft? 2) When the inner eyewall was sustained, was the DEF of latent heating in the inner eyewall larger than outside the inner eyewall? 3) Does the DEF of latent heating and momentum forcing play certain roles in maintaining concentric eyewalls? We use a three-dimensional full-physics WRF model to simulate TC Lekima. The Sawyer-Eliassen equation is used to diagnose the moat downdraft driven by each region's latent heating and momentum forcing. We then perform the DEF diagnoses to calculate the dynamic efficiency of latent heating and momentum forcing for inner and outer eyewalls. The remainder of this paper is organized as follows. Section 2 gives the WRF configuration, the Sawyer-Eliassen

equation framework, and the DEF diagnosis. The TC case overview, WRF model results, are given in section 3. The Sawyer-Eliassen and DEF diagnoses are given in section 4.

The conclusions are given in section 5.



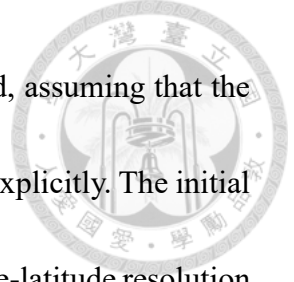


Chapter 2. Methodology

2.1 WRF configuration

The Advanced Research version of the Weather Research and Forecasting Model (WRF-ARW version 3.9; Skamarock et al., 2008) was used to simulate TC Lekima (2019). The WRF simulation was run for 108 hours from 0000 UTC 5 August to 1200 UTC 9 August 2019. Four nested grids were used, with a horizontal grid spacing of 27, 9, 3, and 1 km, and with grid points of 450×300 , 631×481 , 541×541 , and 511×511 , respectively. The innermost 1-km grid started at 0000 UTC on 7 August, one day before TC Lekima was observed by radar at Ishigaki Island. The 3-km and 1-km grids moved with the TC center (see Fig. 1). The 1-km grid was assumed to be able to resolve the convective-scale features and to better represent the inner-core structure. Two-way interaction between inner and outer grids was considered. Fifty-five eta (η) levels were used, and the model top was at 30 hPa. The time step for the outermost domain is 30 seconds.

The physical parameterization schemes used for the WRF simulation of TC Lekima include the Betts-Miller-Janjić cumulus parameterization (Janjić, 1994), the WRF double-moment 6 class (WDM6) microphysics parameterization (Lim & Hong, 2010), the Rapid Radiative Transfer Model (RRTM) longwave parameterization (Mlawer et al., 1997), the Dudhia shortwave parameterization (Dudhia, 1989), and Yonsei University (YSU) planetary boundary layer (PBL) parameterization (Hong et al., 2006). The cumulus



parameterization scheme was only used on the outermost 27-km grid, assuming that the 9-km, 3-km, and 1-km grids were fine enough to resolve convection explicitly. The initial and boundary conditions were from the ERA5 dataset, with a longitude-latitude resolution of 0.25° updated every hour. The sea surfaces temperature was fixed throughout the model simulation period. The output of the 1-km and 3-km grids was at a time interval of 5 minutes.

2.2 Sawyer-Eliassen diagnoses

The Sawyer-Eliassen equation was used to diagnose the secondary circulation of TC Lekima in the axisymmetric framework. Under the assumptions of the axisymmetric vortex, gradient-wind balance, and hydrostatic balance, we can list the gradient balance equation, tangential momentum equation, hydrostatic balance equation, continuity equation, and thermodynamic equation in the cylindrical coordinate as

$$\left(f + \frac{v}{r}\right)v = \frac{\partial\phi}{\partial r}, \quad (1a)$$

$$\frac{dv}{dr} + fu + \frac{uv}{r} = F, \quad (1b)$$

$$\frac{\partial\phi}{\partial z} = \frac{g}{\theta_0}\theta, \quad (1c)$$

$$\frac{\partial ru}{r \partial r} + \frac{\partial \rho w}{\rho \partial z} = 0, \quad (1d)$$

$$\frac{d\theta}{dt} = \frac{\partial\theta}{\partial t} + u \frac{\partial\theta}{\partial r} + w \frac{\partial\theta}{\partial z} = Q, \quad (1e)$$

where $z = \left(\frac{c_p\theta_0}{g}\right)\left(1 - \left(\frac{p}{p_0}\right)^k\right)$ is the pseudoheight vertical coordinate; Q is the



diabatic heating; F is the tangential momentum forcing; u , v , w are the radial, tangential, vertical velocity; $\rho = \rho_0 \left(\frac{p}{p_0}\right)^{\frac{1}{\kappa}-1}$ is the pseudodensity; ϕ is the geopotential; θ is the potential temperature; f is the Coriolis parameter.

Because $u = dr/dt$, we multiply the left-hand side of (1b) with r to obtain

$$r \frac{dv}{dr} + rf \frac{dr}{dt} + v \frac{dr}{dt} = \frac{d}{dt} \left(rv + \frac{1}{2} fr^2 \right) = \frac{dm}{dt}, \quad (2)$$

where $m = rv + \frac{1}{2} fr^2$. Using (2), the left-hand side of (1a) can be written as

$$\begin{aligned} fv + \frac{v^2}{r} &= \frac{1}{r^2} v(rv + fr^2) \\ &= \frac{1}{r^3} \left(rv + \frac{1}{2} fr^2 - \frac{1}{2} fr^2 \right) \left(rv + \frac{1}{2} fr^2 + \frac{1}{2} fr^2 \right) = \frac{1}{r^3} \left(m^2 - \frac{1}{4} f^2 r^4 \right). \end{aligned} \quad (3)$$

Using Eq. (3) and (2), Eq. (1a) and (1b) can be rewritten as

$$\frac{\partial \phi}{\partial r} = \frac{1}{r^3} \left(m^2 - \frac{1}{4} f^2 r^4 \right), \quad (4a)$$

$$\frac{dm}{dt} = \frac{\partial m}{\partial t} + u \frac{\partial m}{\partial r} + w \frac{\partial m}{\partial z} = rF. \quad (4b)$$

We can obtain the thermal-wind equation by combining $\partial/\partial z$ of Eq. (4a) and $\partial/\partial r$ of

Eq. (1c)

$$\frac{g}{\theta_0} \frac{\partial \theta}{\partial r} = \frac{1}{r^3} \frac{\partial m^2}{\partial z}, \quad (5)$$

and its time derivative can be written as

$$\frac{\partial}{\partial t} \left(\frac{g}{\theta_0} \frac{\partial \theta}{\partial r} \right) = \frac{\partial}{\partial t} \left(\frac{1}{r^3} \frac{\partial m^2}{\partial z} \right). \quad (6)$$

We multiply Eq. (4b) by $\frac{2m}{r^3}$ and multiply Eq. (1e) by g/θ_0 , we can express equations as

$$\frac{1}{r^3} \frac{\partial m^2}{\partial t} + \rho u C - \rho w B = \frac{2mF}{r^2}, \quad (7a)$$

$$\frac{g}{\theta_0} \frac{\partial \theta}{\partial t} - \rho u B + \rho w A = \frac{g}{\theta_0} Q, \quad (7b)$$



where

$$A = \frac{g}{\rho\theta_0} \frac{\partial\theta}{\partial z}, \quad (8a)$$

$$B = -\frac{g}{\rho\theta_0} \frac{\partial\theta}{\partial r} = -\frac{1}{\rho r^3} \frac{\partial m^2}{\partial z}, \quad (8b) \quad \text{and}$$

$$C = \frac{1}{\rho r^3} \frac{\partial m^2}{\partial r}, \quad (8c)$$

Based on the continuity equation (1d), the stream function ψ can be defined as

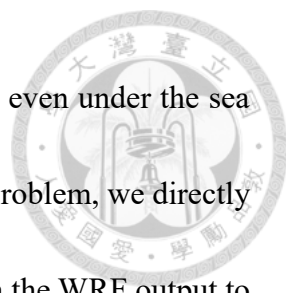
$$(\mathbf{u}, \mathbf{w}) = \left(-\frac{\partial\psi}{\rho\partial z}, \frac{\partial(r\psi)}{r\rho\partial r} \right). \quad (9)$$

We take the derivatives of Eq. (7a) with respect to z and Eq. (7b) with respect to r , then subtract Eq. (7b) with Eq. (7a), and then use Eq. (9). We can obtain the Sawyer-Eliassen equation

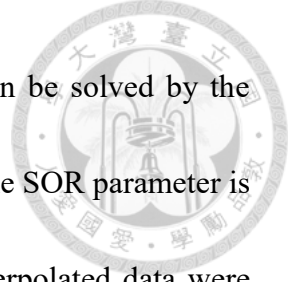
$$\frac{\partial}{\partial r} \left(A \frac{\partial(r\psi)}{r\partial r} + B \frac{\partial\psi}{\partial z} \right) + \frac{\partial}{\partial z} \left(B \frac{\partial(r\psi)}{r\partial r} + C \frac{\partial\psi}{\partial z} \right) = \frac{g}{\theta_0} \frac{\partial Q}{\partial r} - \frac{1}{r^2} \frac{\partial(2mF)}{\partial z}. \quad (10)$$

Diabatic heating includes latent heating only, and the tangential momentum forcing includes friction and turbulence mixing by the PBL scheme.

We used the 3-km domain outputs from the WRF simulation to diagnose the secondary circulation. We interpolated the WRF results into the cylindrical coordinate with an interval of 1 km (from 1 to 800 km) in the radial, with an interval of 400 meters (from 200-meter to 23-km height) in the vertical, and with an interval of 1 degree in the azimuthal. Then, we took the azimuthal average to obtain the axisymmetric structure. Under the pseudoheight structure, the vertical is the pressure coordinate. The minimum sea-level pressure was up to 920 hPa in the simulated Lekima (Fig. 2b). About the grid



points under 920 hPa, the grid point will be close to the sea level or even under the sea level as the radial position approaching the TC center. To avoid this problem, we directly interpolate the height coordinate to the pseudoheight coordinate from the WRF output to the diagnosis domain. Some inaccuracies may exist due to the difference in height locations between the pseudoheight and physical height coordinate. However, these inaccuracies only exist in the region close to the eye, which is a small region. Nonetheless, using this approach, the secondary circulations solved by the Sawyer-Eliassen equation are close to the azimuthal-averaged secondary circulations from the WRF simulation (Fig. 9). The stream function ψ was set to zero at the inner, outer, top, and bottom boundaries. The outer boundary condition setting to $\frac{\partial\psi}{\partial r} = 0$ is the better approach (for example, Wang et al., 2016); however, the outer boundary condition setting to $\psi = 0$ is needed in the DEF diagnoses due to the math feature. To keep the boundary conditions consistent, we set the outer boundary condition to $\psi = 0$ in both Sawyer-Eliassen and DEF diagnoses. The disadvantage is that the diagnosis domain is a closed space. The subsidence caused by the eyewall updraft (the continuity equation) must exist in the region between the eyewall and outer boundary. Because of the limited space, the Sawyer-Eliassen diagnosed upper-level updraft outside the eyewall will be underestimated by the unreal subsidence. To mitigate this problem, we extend the outer boundary location to $r = 800$ km. We considered $AC - B^2 > 0$ for every point in the grid



so that Eq. (10) is an elliptic equation, and the stream function can be solved by the successive over-relaxation method (SOR) with parameter 1.942. If the SOR parameter is appropriate, SOR can reduce iterations hundreds of times. The interpolated data were smoothed by a 1-2-1 smoother 15 times to reduce the numerical instability at the grid point where $AC - B^2 > 0$ was not satisfied. If there is $A < 0$ (static instability) or $C < 0$ (inertial instability) in some grid points after smoothing, we set A or C to 0 at those grid points. The second-order central difference scheme evaluated all of the differential terms in Eq. (10). No staggered grids are used. The convergent condition is that the maximum stream function difference between the adjacent two iterations is smaller than $1 \text{ kg m}^{-1} \text{ s}^{-1}$. Based on the above grid point settings, solving the Sawyer-Eliassen equation per time only took about 30 seconds.

2.3 Dynamic efficiency factor diagnoses

Following Kuo et al. (2019), we consider the following two energy equations that satisfy the Sawyer-Eliassen equation:

$$\frac{dP}{dt} = H - C_{PK}, \quad (11a)$$

and

$$\frac{dK}{dt} = C_{PK} + M, \quad (11b)$$

where P is the total potential energy, K is the total kinetic energy, H is the total latent



heating, M is the total kinetic energy generation rate by momentum forcing, and C is the conversion rate from P to K . These quantities can be expressed as

$$P = \iint c_p T \rho r dr dz, \quad (12a)$$

$$K = \iint \frac{v^2}{2} \rho r dr dz, \quad (12b)$$

$$H = \iint \frac{c_p T Q \rho}{\theta} r dr dz, \quad (12c)$$

$$M = \iint F v \rho r dr dz, \quad (12d)$$

and

$$C_{PK} = \iint \frac{g w \theta \rho}{\theta_0} r dr dz. \quad (12e)$$

After some substitutions, C can be also expressed as

$$C_{PK} = \iint \frac{\eta_H c_p T Q \rho}{\theta} r dr dz + \iint \eta_M F v \rho r dr dz. \quad (13)$$

where η_H is the dynamic efficiency factor (DEF) of latent heating, and η_M is the DEF of momentum. η_H represents the efficiency of converting latent heating into kinetic energy, and η_M represents the ratio of the amount of kinetic energy converted from potential energy to the amount of kinetic energy dissipated by friction. η_H and η_M can be expressed as

$$\eta_H = \frac{g}{\rho c_p \theta_0} \left(\frac{p_0}{p} \right)^{\kappa} \frac{\partial r \chi}{r \partial r}, \quad (14a)$$

and

$$\eta_M = -\frac{2m}{\rho v r^2} \frac{\partial \chi}{\partial z}. \quad (14b)$$

We can obtain χ by solving the Sawyer-Eliassen equation and replacing the right-hand



side (RHS) with baroclinicity and the variable to χ :

$$\frac{\partial}{\partial r} \left(A \frac{\partial(r\chi)}{r\partial r} + B \frac{\partial\chi}{\partial z} \right) + \frac{\partial}{\partial z} \left(B \frac{\partial(r\chi)}{r\partial r} + C \frac{\partial\chi}{\partial z} \right) = \frac{g}{\rho\theta_0} \frac{\partial\theta}{\partial r}. \quad (15)$$

Then, χ , η_H , and η_M at each grid point can be solved. The first term and the second term of RHS of Eq. (13) are the conversion rate by latent heating ($\overline{C_H}$) and by momentum forcing ($\overline{C_F}$), respectively. They represent the total amount of kinetic energy converted from latent heating and momentum forcing in a specific vertical and radial range. We also define the system DEF of latent heating ($\overline{\eta_H}$) and momentum ($\overline{\eta_M}$) to measure the average DEF of latent heating or momentum in a specific vertical and radial range:

$$\overline{\eta_H} = \frac{\overline{C_H}}{H} = \frac{\iint \frac{\eta_H c_p T Q \rho}{\theta} r dr dz}{\iint \frac{c_p T Q \rho}{\theta} r dr dz}, \quad (16a)$$

and

$$\overline{\eta_M} = \frac{\overline{C_M}}{M} = \frac{\iint \eta_M F v p r dr dz}{\iint F v p r dr dz}. \quad (16b)$$

The complete derivation can be found by Kuo et al. (2019). The boundary, grid, and data setting for DEF diagnoses are the same as those in the Sawyer-Eliassen diagnoses for consistency.

Chapter 3. Case Overview



3.1 Observations

According to the JMA best-track data, Typhoon Lekima formed in the western North Pacific (16.9°N, 130.6°E) at 0000 UTC 5 August 2019, then moved west-northward stably from 5 to 10 August with a maximum wind speed of 105 kt before making landfall in China at 1800 UTC on 9 August 2019 (Fig. 2). After landfall, Lekima weakened to a tropical depression, moved northward, and dissipated on 12 August. At 1200 UTC on 8 August, when Lekima was ~400 km east of Taiwan and 150 km southeast of Ishigaki Island, the maximum 10-m wind speed was 105 kt (about 54 ms⁻¹), and the minimum sea-level pressure was 925 hPa (Figs. 2b and 2c).

Both radars observed TC Lekima on Mt. Wufen (RCWF) and Ishigaki Island. Figure 3 shows the reflectivity from radars on Mt. Wufen (with an elevation angle of 0.5°) and on Ishigaki Island (with an elevation angle of 0.2°). At 0605 UTC on 8 August, Lekima showed clear concentric eyewalls. The inner eyewall had a maximum reflectivity of 45 dBZ west of the center, and the outer eyewall had a maximum reflectivity of 40 dBZ (Fig. 3a). The region between the inner eyewall and outer eyewall (i.e. the moat) was composed of a large area of empty reflectivity with some sparse areas of 35-dBZ reflectivity. After 12 hours, Lekima still showed a clear concentric eyewall structure with stronger outer eyewall reflectivity south of the center (Fig. 3b).

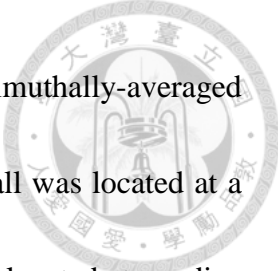



Figure 4 shows Ishigaki Island radar's Hovmöller diagram of azimuthally-averaged reflectivity at $z = 2$ km. At 0600 UTC on 8 August, the inner eyewall was located at a radius of 10 to 20 km from the TC center, and the outer eyewall was located at a radius of 70 to 110 km from the TC center. The outer eyewall contracted for about 20 km from 0600 UTC to 1800 UTC on 8 August. Despite some uneven magnitudes of reflectivity, the position and width of the inner eyewall, moat, and outer eyewall were approximately the same at every azimuthal angle, indicating a high degree of axisymmetry (Figs. 3a and 3b). At 0302 UTC on 9 August, TC Lekima showed a more axisymmetric concentric eyewall structure with uniform reflectivity at each azimuthal angle. The moat was also clear (Fig. 3c). The concentric eyewalls were maintained until one hour before Lekima made landfall in China (Fig. 3d). Overall, the concentric eyewalls of TC Lekima were sustained for about 34 hours during the radar observation period.

3.2 Model results

The TC Lekima's track was well simulated by the WRF model, as shown in Fig. 2a. Throughout the whole simulation time, the simulated track was similar to the observed track. The simulated Lekima moved northeastward slowly on 9 August. The evolution of the simulated maximum wind speed and minimum sea-level pressure was similar to those in the observations (Figs. 2b and 2c), but the simulated Lekima had stronger intensity



than that in the observation. the maximum TC intensity was higher than those in the JMA best-track data after 0600 UTC on 8 August. To be specific, the minimum sea-level pressure is 115 kt and 915 hPa in the simulation, but it is 925 hPa in the JMA best-track data. One potential reason for the larger simulated intensity was the fixed sea surface temperature in the simulation.

Figure 5 shows the horizontal reflectivity structure of the simulated Lekima at $z = 2$ km from 0600 UTC 8 August to 0600 UTC on 9 August. Because 3-km and 1-km domains moved with the TC center in the simulation, we used the domain center as the TC center. At 0600 UTC on 8 August, the simulated Lekima showed a concentric eyewall structure with the inner eyewall located at $r = 30$ to 40 km and the outer eyewall located at $r = 80$ to 140 km. The outer eyewall comprised vigorous convective cells in the downshear-left quadrant and upshear-left quadrants but fewer convective cells south of the center. From 0600 UTC on 8 August to 0600 UTC on 9 August, the outer eyewall was wrapping counter-clockwise, and the comprised convection reflectivity was strengthening, indicating the outer eyewall was enhancing continuously. During the same period, the inner eyewall was contracting slightly. The inner eyewall was located at $r = 20$ to 30 km at 0600 UTC on 8 August. The moat was located at $r = 40$ to 70 km between two eyewalls. The moat had a low echo in the direction with more vigorous convection in the outer eyewall and had an empty echo in the direction with weaker convection in the outer

eyewall.





Figure 6 shows the Hovmöller diagram of azimuthally-averaged reflectivity, tangential wind, and vertical velocity, respectively, at $z = 2$ km. Before 0600 UTC on 8 August, the primary eyewall shows a high reflectivity (> 40 dBZ) and tangential wind ($> 50 \text{ m s}^{-1}$) at $r = 30$ to 40 km (Figs. 6a and 6b). At 0600 UTC, the secondary reflectivity peak was located at $r = 70$ to 130 km with a magnitude of ~ 30 dBZ (Fig. 6a). During 0600 UTC to 1800 UTC on 8 August, the reflectivity, tangential wind, and vertical velocity in the primary eyewall increased, and the primary eyewall contracted to $r = 20$ to 30 km (Fig 6). The secondary reflectivity peak, tangential wind, and vertical velocity further strengthened after 1800 UTC on 8 August, while the reflectivity, tangential wind, and vertical velocity of the primary eyewall weakened (Fig 6). From 0600 UTC on 8 August to 0600 UTC on 9 August, the moat with empty reflectivity, weaker updraft (compared to eyewalls), and slight downdraft was apparent (Fig 6a and 6c). Because the concentric eyewall structure, including two reflectivity and vertical wind peak of two eyewalls and downdraft and empty reflectivity of the moat, was apparent at 0600 UTC on 8 August, we define this time is the secondary eyewall formation time. These features were apparent until 0600 UTC on 9 August, so the lifetime of the concentric eyewall structure of the simulated Lekima was about 24 hours.

Compared to the observation, the inner eyewall of the simulated Lekima was wider



by ~ 10 km. Thus, the simulated Lekima exhibited a thinner moat. From Fig. 6a, the simulated double reflectivity peak structure was sustained for about 24 hours (from 0600 UTC on 8 August to 0600 UTC on 9 August), which is shorter than that in the observation (34 hours). Despite these differences, both observation and simulation showed long-lived concentric eyewall duration. According to the threshold defined by Yang et al. (2013), the concentric eyewalls sustained for over 20 hours were classified as concentric eyewall maintenance (CEM) group, which had long-lived concentric eyewall structures. Both observation and simulation were classified as this group. Despite the simulated Lekima exhibiting shorter concentric eyewall duration (24 hours), the duration was still far longer than the mean concentric eyewall duration (16 hours) of TCs in the western North Pacific (Yang et al., 2021).

3.3 Axisymmetry

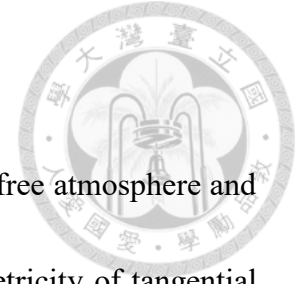
Following Miyamoto and Takemi (2013) and Kuo et al. (2019), the axisymmetry of the simulation was examined by:

$$\gamma(r, z, t) \equiv \frac{\bar{\phi}(r, z, t)^2}{\bar{\phi}(r, z, t)^2 + \int_0^{2\pi} \phi'(r, z, t)^2 d\lambda / 2\pi}, \quad (17)$$

where ϕ is arbitrary variable, with the overbar denoting the azimuthal-averaged variable, the prime denoting the perturbation variable, and the λ represents the azimuthal angle.

The axisymmetry of the system can be represented as:

$$\bar{\gamma}(t) = \frac{1}{R(Z-Z_0)} \sum_{z=Z_0}^Z \sum_{r=0}^R \gamma(r, z, t). \quad (18)$$



Z_0 , Z and R are set to 1.5, 12, and 150 km to focus on the range of free atmosphere and the concentric eyewalls. Figure 7 shows the evolution of axisymmetry of tangential wind, reflectivity, and potential vorticity in the simulation. The axisymmetry of tangential wind was over 0.9 after 0000 UTC on 8 August. The axisymmetry of potential vorticity increased from 0.5 to 0.6 during the concentric eyewall period. The high axisymmetry of potential vorticity was mainly distributed in the inner core (not shown). The high axisymmetry of potential vorticity inside the outer eyewall ($r < 70$ km) was up to 0.77. The high axisymmetry allows us to perform the Sawyer-Eliassen diagnoses and the DEF computations under axisymmetric vortex assumption. Despite the concentric-eyewall duration difference between the observation and simulation, the concentric eyewalls were maintained in both the observation and simulation between 0600 UTC on 8 August to 0600 UTC on 9 August. This 24-h period was chosen to perform the Sawyer-Eliassen diagnoses and DEF calculations.

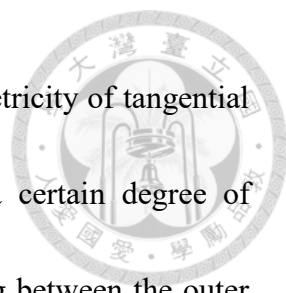


Chapter 4. Diagnosis Results

4.1 Results of Sawyer-Eliassen diagnoses


We distinguished the inner core of TC Lekima into the inner eyewall, moat, and outer eyewall regions to investigate their latent heating and momentum forcing contributions to the moat downdraft. Then, the moat downdraft driven by forcing terms in each region can be obtained by solving the Sawyer-Eliassen equation separately. Nine forcing conditions were used to diagnose the corresponding secondary circulation responses. Table 1 shows the latent heating (Q) and momentum forcing (F) for each diagnosis experiment. Diag1 used the latent heating and momentum forcing in the entire diagnosed domain. Diag2 (Diag3) used only the latent heating (momentum forcing) inside the concentric eyewalls. The experiment from Diag4 to Diag6 (Diag7 to Diag9) used the latent heating (momentum forcing) only in the inner eyewall, moat, and outer eyewall, respectively. Except for Diag1, the forcing term outside the outer eyewall was not used.

The ranges of the inner eyewall, moat, and outer eyewall regions were defined by the spatial distribution of latent heating. The region where the latent heating was closest to the eye and with a magnitude larger than zero was defined as the inner eyewall. The region where the latent heating was outside the inner eyewall and with a magnitude larger than $4 \times 10^{-4} \text{ K s}^{-1}$ was the outer eyewall. The remainder region between these two eyewalls was the moat. The whole range of the vertical was used in each diagnosis (from



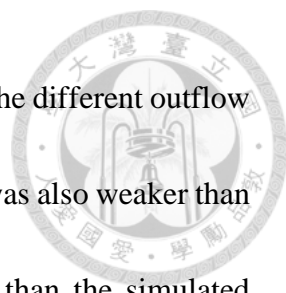
200 m to 23 km, with an interval of 400 m). Although the axisymmetry of tangential wind and potential vorticity reached 0.9 and 0.7, respectively, a certain degree of asymmetry still existed in TC Lekima. Distinguishing latent heating between the outer eyewall and outer rainband was ambiguous after taking the azimuthal average. Subjective analysis was used to find the boundary separating the outer eyewall from the outer rainband at every diagnosis time. The azimuthally-averaged vertical velocity, tangential wind, and horizontal distributions of reflectivity at multiple altitudes were used in the subjective analyses. Because of the assumptions of balance dynamics for the Sawyer-Eliassen equation, a slowly evolving TC vortex must be assumed. The small-scale and high-frequency signals in the azimuthally-averaged stabilities and forcing terms were filtered out by the 1-h temporal running mean (from -30 minutes to +30 minutes for the diagnosis time).

Figure 8 shows the azimuthally-averaged latent heating and momentum forcing in different diagnoses (panel b to panel i for Diag2 to Diag9) and vertical velocity from the WRF simulation (panel a) at 1300 UTC 8 August 2019. At this time, simulated inner eyewall and outer eyewall updrafts existed between $r = 20$ and 40 km and $r = 70$ and 140 km, respectively. At the same time, a moat downdraft was present below $z = 13$ km (Fig. 8a). Inside the concentric eyewalls, the locations of the updraft (downdraft) and latent heating (cooling) highly overlapped (Fig. 8b). Thus, strong latent heating was identified



in the inner and outer eyewall regions (Figs. 8d and 8f). The the moat had latent cooling (Fig. 8e), but the moat may still have weak latent heating at other times. The convective cells in the moat were weaker than those in the two eyewalls because of the short filamentation time in the moat (Kuo et al. 2012; Qin et al., 2021). Short filamentation time is a typical feature of the moat and can strain convective cells to enhance the entrainment effect and weaken convection. Thus, we still kept these convective cells in the moat region. The momentum forcing was concentrated within the boundary layer and was distinguished into the inner eyewall, moat, and outer eyewall (Figs. 8c, g, h, and i).

Figure 9 shows the two secondary circulations from the Sawyer-Eliassen diagnoses, the azimuthally-averaged WRF simulation, the difference at 1300 UTC on 8 August 2019, and the corresponding correlation coefficients computed along the time dimension (289 diagnosed times). The overall patterns and magnitudes of the two secondary circulations, including the inner- and outer-eyewall updrafts, and the low-level inflow, had high similarities. However, a discernible difference existed at the upper levels. The diagnosed upper-level outflow was smaller than the simulated outflow (Fig. 9f). The diagnosed outflow had two peaks produced by inner-eyewall and outer-eyewall updraft, but there was only a peak outside the outer-eyewall in the simulated outflow (Fig. 9b and 9d). Because the outward pressure gradient force existed in the WRF simulation (not shown), the gradient-wind balance was not satisfied. The Sawyer-Eliassen equation obtained weak

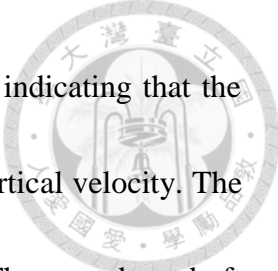


outflow under the gradient-wind balance, and this reason may cause the different outflow structures. The diagnosed inner-eyewall and outer-eyewall updrafts was also weaker than the simulated updrafts, but the diagnosed downdraft was stronger than the simulated downdraft (Fig. 9e). The large positive correlation coefficients (larger than 0.8) of secondary circulation were distributed widely in the concentric eyewall structure ($r > 20$ km and $r < 160$ km). At the upper levels ($z > 14$ km and $r > 130$ km) where the gradient-wind balance was not satisfied, the correlation coefficients associated with vertical velocity were smaller than 0.8. In the eye ($r < 20$ km), the correlation coefficients associated with secondary circulations were nearly zero or negative. It may be caused by some uncertainty of defining the simulated TC center. This uncertainty may introduce some asymmetry to the eye region.

Figure 10 shows the vertical velocity of each diagnosis at 1300 UTC on 8 August 2019. To quantify the contributions to the moat downdraft by the latent heating in each region, the mass fluxes of the moat downdrafts (inside the black contour in Fig. 10) are computed by:

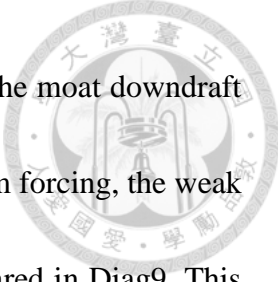
$$\mu = 2\pi \iint \rho_0 w r dr dz. \quad (19)$$

Then, the ratios of the moat downdraft mass fluxes in diagnoses considering latent heating (i.e., Diag1, Diag2, and Diag3 to 5) to the moat downdraft mass flux in Diag2 (considering latent heating in the concentric eyewalls only) are computed. The vertical



velocity in Diag1 was similar to that in Diag2 (Figs. 10a and 10b), indicating that the latent heating in the concentric eyewalls mainly contributes to the vertical velocity. The moat and eye downdrafts were stronger in Diag2 than those in Diag1. The moat downdraft mass flux in Diag1 was about 95% times the mass flux in Diag2. The excessive moat downdraft was offset by the updraft that responded to the momentum forcing in Diag3. The momentum forcing, mainly distributed in the boundary layer, induced low-level inflow that converged and converted to an updraft in the inner core to offset the excessive moat downdraft.

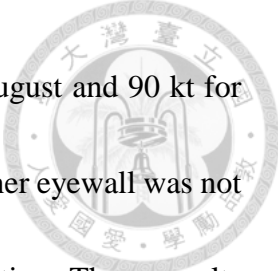
Downdrafts existed in the moat regions in Diag4, Diag5, and Diag6. The moat downdrafts concentrated at low levels in Diag4 and Diag5, while the moat downdraft concentrated at the upper level in Diag6. After the outer eyewall formed, lots of moist air was lifted into the outer eyewall, and some air was forced downward inside the outer eyewall. This is similar to the flow ejected into the eye from the eyewall (Houze et al., 2007), and it can cause adiabatic warming and a decrease in relative humidity. Therefore, the latent cooling processes, including evaporation, melting, and sublimation could induce the moat downdraft at the lower to middle levels (Figs. 8e and 10e). The moat downdraft in Diag4 was the compensative downdraft of the eyewall updraft produced by the inner eyewall latent heating. For the relative contributions to the moat downdraft, the mass flux ratios in Diag4, Diag5, and Diag6 were about 32%, 21%, and 47%, respectively.



This indicates that the latent heating in two eyewalls contributed to the moat downdraft more than the local latent cooling. For the responses to the momentum forcing, the weak downdraft in the moat only appeared in Diag7, but the updraft appeared in Diag9. This reveals that the momentum forcing did not directly contribute to the moat's subsidence.

We further examine the relative contributions to the moat downdraft during the period when the concentric eyewalls were maintained. Figure 11 shows the evolution of the moat mass flux ratios of Diag4, Diag5, and Diag6 from 0600 UTC on 8 August 2019 to 0600 UTC on 9 August 2019. Shortly after concentric eyewalls forms (0600 UTC to 0800 UTC on 8 August), the moat downdraft was mainly driven by Diag6 and Diag5 (Fig. 11a). Between 0800 UTC and 1800 UTC on 8 August, the moat downdraft was mainly driven Diag6, with a secondary contribution by the Diag4, and with the smallest contribution by Diag5 (Fig. 11a). As time went on, the simulated moat downdraft mass flux decreased, the latent heating in the inner eyewall decreased, the latent cooling in the moat decreased, but the latent heating in the outer eyewall increased, indicating the progression of the ERC (Fig. 11b). Between 1800 UTC on 8 August and 0600 UTC on 9 August, both the moat downdraft driven by Diag4 and Diag5 decreased to weak positive or negative downdraft contribution (Fig. 11a). The moat downdraft driven by Diag6 strengthened and became to the main contributor.

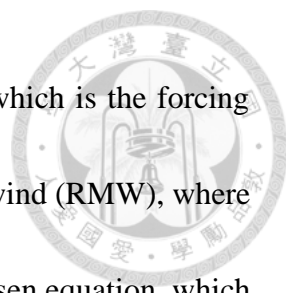
The tangential wind speed in the inner eyewall decreased for only 7 kt during the



concentric eyewall maintenance period (97 kt for 0600 UTC on 8 August and 90 kt for 0600 UTC on 9 August; Fig. 6c), indicating that the strength of the inner eyewall was not affected substantially by the outer eyewall formation in this simulation. These results differ from the previous studies, which indicated that the maximum wind speed in the inner eyewall started to decrease hours before the outer eyewall formation and decreased more largely after the outer eyewall formation (e.g., Zhu and Zhu, 2014). After the outer eyewall formation, some moisture was intercepted at the outer eyewall and caused the inner eyewall to dissipate. To maintain the tangential wind speed at the inner eyewall where the moisture was restricted, the efficiency of converting the latent heat release into kinetic energy must be significant. Therefore, we use the DEF diagnoses to investigate this dynamic efficiency in the inner eyewall.

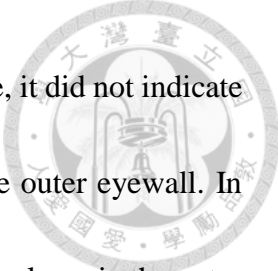
4.2 Results of dynamic efficiency factor diagnoses

The latent heating and momentum forcing in the whole domain were used in the DEF diagnoses. Figure 12 presents the DEF of latent heating and momentum, and baroclinicity at 1300 UTC on 8 August 2019. Overall, the DEF of latent heating was larger at upper levels than that at lower levels. The DEF of latent heating at the inner eyewall was also higher than that outside the inner eyewall at the same altitude. For example, the DEF of latent heating at $z = 10$ km in the inner eyewall was up to 12%. Still, at the same altitude



and $r = 120$ km, it reached only 6% (Fig. 12a). The baroclinicity, which is the forcing term of DEF, was distributed mainly inside the radius of maximum wind (RMW), where the inertial stability was large. Due to the nature of the Sawyer-Eliassen equation, which is an ellipse equation, the forcing term was restricted in the radial in a high inertial stability condition. It caused the high DEF of latent heating in the inner eyewall. These results agree with previous studies. If the convection occurs inside the RMW, the latent heating can form the warm core and cause the TC to intensify effectively (Rogers et al., 2013). Kuo et al. (2019) also indicated that the DEF of latent heating inside the RMW was higher than that outside the RMW in TC Haiyan (2013). This configuration caused the volume-integrated kinetic energy to increase rapidly. The momentum forcing was mainly distributed inside the boundary layer with $z < 1.5$ km. In the boundary layer, the DEF of momentum was negative with a large magnitude, and the magnitude was larger in the inner eyewall than that in the outer eyewall, indicating some kinetic energy was generated to offset part of the dispersed tangential wind.

In Fig. 12a and Fig. 12b, the magnitudes of η_H and η_M are higher in the inner eyewall than those outside the inner eyewall. However, η_H or η_M has no particular patterns in the outer eyewall. In other words, there were fewer impacts on η_H or η_M in the outer eyewall when the outer eyewall existed. One possible reason is that the forcing term of Eq. (15) is baroclinicity rather than diabatic heating or friction. Even though latent



heat release in the outer eyewall had magnitudes at the diagnostic time, it did not indicate that outer eyewall convection had contributions on η_H or η_M at the outer eyewall. In this simulation, the warm core (potential energy) caused by latent heat release in the outer eyewall was much weaker than the warm core in the inner eyewall (Fig. 12c). The baroclinicity was mainly distributed in the inner eyewall, but the baroclinicity in the outer eyewall was very weak. In addition, the inertial stability was high in the inner eyewall, so the spatial variation of χ (i.e., η_H and η_M) mainly distributed in the inner eyewall, but could not extend to the outer eyewall. The χ was smooth in the outer eyewall, so the η_H and η_M had little changes.

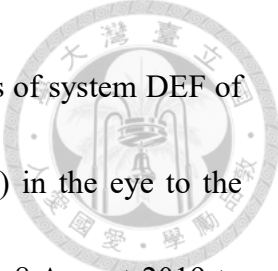
To evaluate the amount of converted energy and relative contribution to the inner-eyewall tangential wind by latent heating or momentum forcing, we computed the conversion rate by latent heating ($\overline{C_H}$) and momentum forcing ($\overline{C_M}$). Figure 13 shows the conversion rate by latent heating and momentum forcing at each grid point (C_H and C_M ; variables inside the integrals of $\overline{C_H}$ and $\overline{C_M}$), as well as the conversion rate by latent heating and momentum forcing in the inner eyewall ($\overline{C_H}$ and $\overline{C_M}$). The integration ranges for the $\overline{C_H}$ and $\overline{C_M}$ are horizontally from $r = 0$ to 40 km and vertically from $z = 0$ to 15 km to cover the entire inner eyewall. The C_H was distributed mainly from $z = 1.5$ to 15 km with a large magnitude in the inner eyewall, but C_M was distributed only below 2 km with a small magnitude in the inner eyewall and moat (Figs. 13a and 13b). Both C_H

and C_M were positive, indicating that both latent heating and momentum forcing were converting potential energy to kinetic energy.



Since the spatial distribution of warm core and tangential wind results from thermal wind balance (Zhang et al., 2000), the energy conversion can be explained by the thermal wind balance adjustment. For the C_H , the latent heating releases in the inner eyewall and the warm core are effectively enhanced in a high inertial stability condition. The enhanced warm core adjusts the potential energy to the tangential wind by secondary circulation to maintain thermal wind balance. For example, 15% of latent heat release can be converted into kinetic energy at the upper level of the inner eyewall. For the C_M , the tangential wind decreases because of friction in the boundary layer. The potential energy (warm core) is converted into kinetic energy (tangential wind) and also by secondary circulation to maintain the thermal wind balance. For example, about 30% of the lost kinetic energy is compensated within the boundary layer of the inner eyewall. By the way, the NOAA's WP-3D aircraft observations showed that over 80 m s^{-1} wind speed existed at 450-m flight level in Hurricane Hugo (1989; Marks et al., 2008). The DEF of momentum may play a role so that such a high wind speed can exist within the boundary layer.

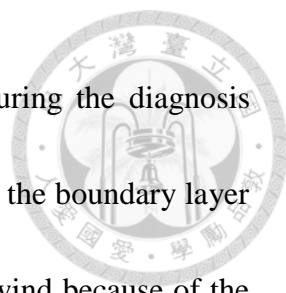
Figure 13c shows that $\overline{C_H}$ was about an order larger than $\overline{C_M}$, indicating that latent heating was the primary source of the inner eyewall tangential wind. After 1800 UTC on 8 August, the $\overline{C_H}$ decreased because Lekima was slightly weakening (Fig. 6b) and the



DEF of latent heating also decreased. Figure 14 shows the time series of system DEF of latent heating ($\bar{\eta}_{H40}$ and $\bar{\eta}_{H150}$) and momentum ($\bar{\eta}_{M40}$ and $\bar{\eta}_{M150}$) in the eye to the inner eyewall and the moat to the outer eyewall from 0600 UTC on 8 August 2019 to 0600 UTC on 9 August 2019. For the system DEF from the eye to the inner eyewall (from the moat to the outer eyewall) with the subscript 40 (150), the radial integration ranges are from 0 to 40 km (40 to 150 km). For the system DEF of latent heating (momentum) with subscript H (M), the vertical integration range is from 1.5 to 15 km (0.2 to 1.5 km). Both the magnitude of $\bar{\eta}_{H40}$ and $\bar{\eta}_{M40}$ decreased after 1800 UTC on 8 August. Since the minimum sea-level pressure of simulated Lekima was weakening, the strength of the warm core and the baroclinicity was also decreasing (Fig. 2b). The maximum wind speed was decreasing after 2100 UTC on 8 August (Fig. 2c), so the inertial stability was decreasing. The magnitude of DEF of latent heating and momentum also decreased.

The system DEF of latent heating at the inner eyewall ($\bar{\eta}_{H40}$) was much higher than outside the inner eyewall ($\bar{\eta}_{H150}$). Albeit a slight weakening of the TC intensity after 1800 UTC on 8 August, $\bar{\eta}_{H40}$ was still higher than $\bar{\eta}_{H150}$. During this period, the outer eyewall developed because of sufficient moisture supply. Despite the cutoff effect by the outer eyewall causing the inner eyewall wind speed to decrease slightly, the double wind speed peak was still maintained by the high DEF of latent heating (Fig. 6b and Fig. 13c).

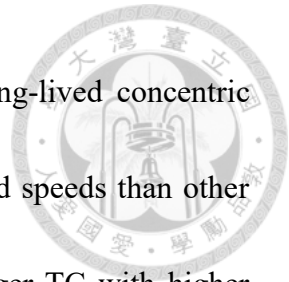
Before 0600 UTC on 8 August, the strength of the inner eyewall increased due to the high



moisture supply (Fig. 2b). $\bar{\eta}_{M40}$ was 50% greater than $\bar{\eta}_{M150}$ during the diagnosis period (Fig. 14b), implying that the inner eyewall tangential wind in the boundary layer can be sustained relatively easier than the outer eyewall tangential wind because of the more kinetic energy compensated by the warm core. In the moisture-restricted condition, this effect has the benefit that the compensative tangential wind can pick up moisture from the sea surfaces just outside the inner eyewall or moat and supply moisture to the inner eyewall convection. Then, the latent heat release can be converted into the inner eyewall kinetic energy by the DEF of latent heating. Though the inner eyewall tangential wind was not contributed primarily by the conversion rate by momentum forcing, the DEF of momentum may still positively impact the inner eyewall convection by the above mechanism.

Based on the above analyses of DEF, we can infer that the inner eyewall wind speed can still be maintained in a strong TC. Because of the thermal wind balance, the faster inner eyewall wind speed accompanies a stronger warm core and thus causes a larger baroclinicity. The larger baroclinicity induces a larger DEF of latent heating in the inner eyewall under a higher inertial stability condition. Therefore, the efficiency of converting latent heating into tangential wind speed is larger, and the inner eyewall wind speed can be maintained easier. This inference is consistent with the statistical analysis based on the satellite microwave observations of TCs in the western North Pacific basin during 1997–

2011 by Yang et al. (2013). They indicated that the TCs with long-lived concentric eyewall structures (longer than 20 hours) had larger maximum wind speeds than other TCs with concentric eyewalls. From the DEF perspective, a stronger TC with higher inertial stability and a stronger warm core makes maintaining the inner eyewall wind speed easier with a higher DEF of latent heating and momentum. The long-lived concentric eyewalls are more likely to exist in more intense TCs.




Chapter 5. Conclusions and future work



5.1 Conclusions

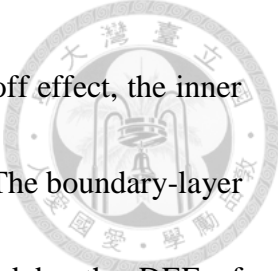
Although ERC is a common phenomenon in intense TCs, the time period to complete an ERC varies. TCs in the WNP took about 16 hours on average to complete an ERC, but one-fourth of these TCs took more than 20 hours and maintained long-lived concentric eyewalls with a large moat. Typhoon Lekima (2019) had long-lived concentric eyewalls for about 34 hours. This study investigates the maintenance mechanism of the long-lived concentric eyewalls of TC Lekima from an axisymmetric perspective. First, this study used a three-dimensional full-physics WRF model with the nested domain grid size down to 1 km to simulate TC Lekima. Then, we used the Sawyer-Eliassen diagnoses and dynamic-efficiency-factor diagnoses to investigate the possible maintenance mechanisms.

In the Sawyer-Eliassen diagnoses, the moat downdraft in the upper levels was mainly produced by the heating response in the outer eyewall. In contrast, the heating response in the inner eyewall and moat mainly produced the moat downdraft in the lower to middle levels. During the concentric eyewall maintenance, the moat downdraft was contributed primarily by latent heating in the inner and outer eyewall but contributed secondarily by latent cooling in the moat. When the outer eyewall strengthens, the relative contribution of the moat downdraft by outer eyewall latent heating increases, and the contribution by



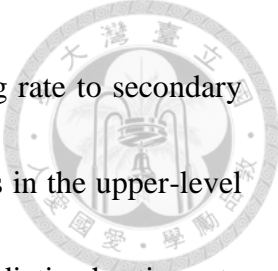
moat latent cooling decreases. Although the concentric eyewalls had been maintained for 24 hours, the inner eyewall latent heating and tangential wind decreased slightly, indicating that the inner eyewall convection can be maintained and was still vigorous under the moisture-restricted condition.

In the DEF diagnoses, the DEF of latent heating and momentum in the inner eyewall were larger than in the outer eyewall. High latent heating and momentum DEF under the moisture-restricted condition can maintain the inner-eyewall wind speed. The kinetic energy in the inner eyewall was mainly from the latent heat release. Although the conversion rate by momentum forcing is an order of magnitude smaller than the conversion rate by latent heating, the conversion rate by momentum forcing may play an indirect role in concentric eyewall maintenance. Since the large negative conversion rate by momentum forcing is concentrated within the boundary layer in the inner eyewall, the tangential wind weakened by friction can be compensated. The compensative tangential wind can pick up moisture from the sea surface in the wide moat and supply moisture to the inner eyewall convection. In a more intense TC with a larger baroclinicity (i.e., warm core) and inertial stability, the DEF of latent heating and momentum in the inner eyewall will be larger, and the above maintenance mechanism will be more noticeable. This inference supports the statistical results by Yang et al. (2013) that long-lived concentric eyewall TCs are more intense than other TCs with concentric eyewalls. Although the



inner eyewall must eventually weaken due to the outer eyewall's cutoff effect, the inner eyewall wind speed can be maintained by the DEF of latent heating. The boundary-layer tangential wind, which can pick up moisture, can be compensated by the DEF of momentum. This study highlights that high DEF of latent heating benefits concentric eyewall maintenance. In addition, the large amount of latent heating also has benefits inherently. Kuo et al. (2022) indicated that the inner boundary layer eyewall pumping strengthens if the dimensionless moat size is larger than 4. The dimensionless moat size of simulated Lekima was up to 18 when the concentric eyewall formed. That the enlarged inner eyewall pumping enhances the inner eyewall latent heating may prolong the concentric eyewall duration.

Although the above discussion gives the mechanism of long-lived concentric eyewall maintenance, there is still some uncertainty in the diagnoses. The diagnoses have gradient-wind balance and hydrostatic balance assumptions, but the assumption may not be satisfied in the boundary layer inflow and upper-level outflow regions. Some adjustment of static stability (A) and inertial stability (C) was used in these two regions so that the Sawyer-Eliassen equation and DEF equation can converge, so there are difficulties in accurately estimating secondary circulations by the Sawyer-Eliassen equation. Only latent heat release is involved in the diabatic heating rate in this study. Although latent heat release is the main composition of the diabatic heating rate in a

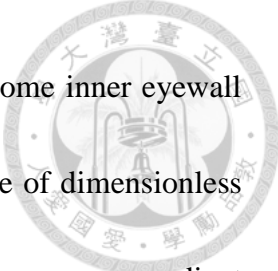


strong TC, there is still some contribution from the radiative heating rate to secondary circulations. For example, the radiative cooling effect may play roles in the upper-level outflow and updraft. The relative impacts of latent heating rate and radiative heating rate have yet to be discussed in this study, so there is still some uncertainty on the contributions of secondary circulations from the radiative heating rate. In addition, this study used the WRF model, which is a complex and full-physics model, to simulate TC Lekima. There are some differences between the simulation results and the reality observations. The duration of concentric eyewall maintenance is 24 hours in the simulation. That duration conforms to the CEM group (duration > 20 hours) in Yang et al. (2013). However, the duration was up to 34 hours in the observations. In the tests of this study, the duration of concentric eyewall maintenance was prolonged from 10 hours to 24 hours when we modified the time step from 75 to 30 seconds. This difference shows the high uncertainty in the model simulations. Changing the microphysics parameterization can also affect the duration of concentric eyewall maintenance. WDM6 was used in the Lekima simulation. Though WDM6 is a double-moment microphysics parameterization scheme, it only considers the mixing ratio rather than the numbers in the ice-phase particles. WDM6 may have varied performance along different simulations. This problem shows uncertainties in microphysics parameterization.



5.2 Future work

Although the Sawyer-Eliassen and DEF diagnoses support the above concentric eyewall maintenance mechanisms, some limitations and revision must be considered. The Sawyer-Eliassen equation can also investigate tangential wind tendency $\left(\frac{\partial v}{\partial t}\right)$ and temperature tendency $\left(\frac{\partial \theta}{\partial t}\right)$. We can obtain the tangential wind tendency and temperature tendency by substituting the solved secondary circulations into the tangential momentum equation and thermodynamic equation, respectively. The completeness of this study can increase. This study used the outer boundary condition $\psi = 0$ in the Sawyer-Eliassen diagnoses. This boundary condition may lead to underestimating the updraft outside the eyewall. This problem can be avoided by changing the outer boundary condition to $\frac{\partial \psi}{\partial r} = 0$. In addition, Eq. (9) can change the vertical velocity to the stream function. We can change the bottom boundary condition by this stream function. This method can avoid the error caused by the discrepancy in thermal-wind balance at the boundary layer. Since the balanced flow is considered in the diagnoses, the physical processes with the unbalanced flow in the boundary layer are not involved in the above mechanisms. We can follow the method posted by Ji and Qiao (2023), solving the extended Sawyer-Eliassen equations. These equations involved balanced and unbalanced parts based on different forcing terms. The latter equation considers the unbalanced effect. Estimating boundary layer inflow would be better if we solve the latter equation. Any processes that



help maintain inner eyewall convection and tangential wind can become inner eyewall maintenance mechanisms. Kuo et al. (2022) highlight the importance of dimensionless moat size, which combines the effect of the moat size and the vortex pressure gradient force to accelerate the unbalanced radial inflow and enlarge the inner boundary layer eyewall pumping for inner eyewall convection maintenance.

Because of the axisymmetric vortex assumption in the diagnoses, the above mechanisms are only for the axisymmetric perspective. We can follow the method posted by Hirano et al. (2022). They consider the asymmetric forcing terms, composed of asymmetric wind speed and potential temperature, to better estimate the TC secondary circulation. The axisymmetric vortex assumption is the limitation of the Sawyer-Eliassen equation. Asymmetric processes also play certain roles in concentric eyewall maintenance, such as barotropic instability and partial cutoff effect (Tsujino et al., 2017; Lai et al., 2021). The maintenance of the inner eyewall is vital to the maintenance of concentric eyewalls. We can also abandon the Sawyer-Eliassen equation and do budget analyses of the WRF simulation results directly. For example, we can use the absolute angular momentum budget analysis to investigate which mechanism can help maintain the tangential wind in the inner eyewall, and we can also use the vertical momentum budget analysis to inspect which mechanism can help maintain the convective updrafts in the inner eyewall. All in all, future research will investigate the physical processes related

to unbalanced flow or asymmetric eddies to understand the concentric-eyewall maintenance mechanism better.

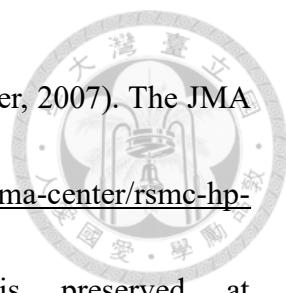


Acknowledgments

The radar data used in this study were provided by the Taiwan Central Weather Bureau (CWB) and Japan Meteorological Agency (JMA). The WRF outputs were post-processed by wrf-python (Ladwig, 2017), and the radar data were post-processed by Py-ART (Helmus & Collis, 2016). This research is supported by the Ministry of Science and Technology of Taiwan under Grants 111-2111-M-002-014 and 111-2123-M-002-014.

Open Research

Version 3.9 of the Advanced Research version of the Weather Research and Forecasting Model (WRF-ARW) used for generating the TC Lekima simulation data is developed openly at <http://dx.doi.org/10.5065/D6MK6B4K> (login with e-mail is needed) and preserved at <http://dx.doi.org/10.5065/D68S4MVH> (Skamarock et al., 2008). Version 1.3.4.1 of wrf-python used for postprocessing WRF data is preserved and developed openly at <https://doi.org/10.5065/D6W094P1> (Ladwig et al., 2017). Version 1.14.1 of The Python ARM Radar Toolkit (Py-ART) used for processing RCWF radar data is preserved at <https://doi.org/10.5334/jors.119> (Helmus & Collis, 2016). Figures in this study were



generated by version 3.5.3 of Matplotlib (Caswell et al., 2022; Hunter, 2007). The JMA best-track data is preserved at <https://www.jma.go.jp/jma/jma-eng/jma-center/rsmc-hp-pub-eg/besttrack.html>. The ERA5 global reanalysis data is preserved at <https://cds.climate.copernicus.eu/cdsapp#!/dataset/reanalysis-era5-single-levels?tab=overview> and <https://cds.climate.copernicus.eu/cdsapp#!/dataset/reanalysis-era5-pressure-levels?tab=overview> (Hersbach et al., 2020). The software solving Sawyer-Eliassen equation and dynamic efficiency factor can be found at <https://github.com/fish5045/SEES>.

Reference



Caswell, T., Lee, A., Droettboom, M., De Andrade, E. S., Hoffmann, T., Klymak, J., et al.

(2022). matplotlib/matplotlib: REL: v3.5.3 (version 3.5.3) [software]. Zenodo.

<https://doi.org/10.5281/zenodo.6982547>

Eliassen, A., & BOLIN, B. (Eds.). (1959). On the formation of fronts in the atmosphere.

In *The Atmosphere and the Sea in Motion* (Rossby Memorial Volume, pp. 277-287).

New York, NY: The Rockefeller Institute Press. <https://doi.org/10.1016/0146->

[6313\(60\)90019-8](https://doi.org/10.1016/0146-6313(60)90019-8)

Eliassen, A. (1964). On the vertical circulation in frontal zones. *Geofys. publ*, 24, 147-

160.

Guimond, S. R., Reasor, P. D., Heymsfield, G. M., & McLinden, M. M. (2020). The

dynamics of vortex Rossby waves and secondary eyewall development in

Hurricane Matthew (2016): New insights from radar measurements. *Journal of the*

Atmospheric Sciences, 77, 2349-2374. <https://doi.org/10.1175/JAS-D-19-0284.1>

Helmus, J.J., & Collis, S.M. (2016). The Python ARM Radar Toolkit (Py-ART), a library

for working with weather radar data in the Python programming language (version

1.14.1). *Journal of Open Research Software*. 4(1), p.e25.

<https://doi.org/10.5334/jors.119>

Hersbach, H, Bell, B, Berrisford, P, et al. (2020) The ERA5 global reanalysis. *Quarterly*

Journal of the Royal Meteorological Society. 146, 1999–2049.

<https://doi.org/10.1002/qj.3803>



Hirano, S., K. ITO, H. Yamada, S. Tsujino, K. Tsuboki, & C.-C. Wu. (2022) Deep Eye

Clouds in Tropical Cyclone Trami (2018) during T-PARCII Dropsonde

Observations. *Journal of the Atmospheric Sciences*, 79, 683-703.

<https://doi.org/10.1175/JAS-D-21-0192.1>

Hong, S.-Y., Noh, Y., & Dudhia, J. (2006). A new vertical diffusion package with an

explicit treatment of entrainment processes. *Monthly Weather Review*, 134, 2318-

2341. <https://doi.org/10.1175/MWR3199.1>

Houze, R. A., Jr, Chen, S. S., Smull, B. F., Lee, W.-C., & Bell, M. M. (2007). Hurricane

intensity and eyewall replacement. *Science*, 315, 1235-1239.

<https://doi.org/10.1126/science.1135650>

Hunter, J. D. (2007). Matplotlib: A 2D Graphics Environment. *Computing in Science &*

Engineering, 9(3), 90-95. <https://doi.org/10.1109/MCSE.2007.55>

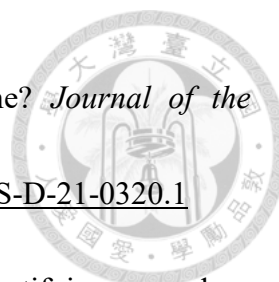
Janjić, Z. I. (1994). The step-mountain eta coordinate model: Further developments of the

convection, viscous sublayer, and turbulence closure schemes. *Monthly Weather*

Review, 122, 927-945. [https://doi.org/10.1175/1520-](https://doi.org/10.1175/1520-0493(1994)122%3C0927:TSMECM%3E2.0.CO;2)

[0493\(1994\)122%3C0927:TSMECM%3E2.0.CO;2](https://doi.org/10.1175/1520-0493(1994)122%3C0927:TSMECM%3E2.0.CO;2)

Ji, D., & Qiao F. (2023). Does Extended Sawyer–Eliassen Equation Effectively Capture



the Secondary Circulation of a Simulated Tropical Cyclone? *Journal of the Atmospheric Sciences*, 80, 871-888. <https://doi.org/10.1175/JAS-D-21-0320.1>

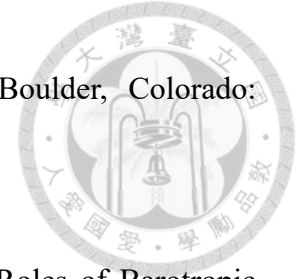
Kossin, J. P., & Sitkowski, M. (2009). An objective model for identifying secondary eyewall formation in hurricanes. *Monthly Weather Review*, 137, 876-892. <https://doi.org/10.1175/2008MWR2701.1>

Kuo, H.-C., Chang, C.-P., Yang, Y.-T., & Jiang, H.-J. (2009). Western North Pacific typhoons with concentric eyewalls. *Monthly Weather Review*, 137, 3758-3770. <https://doi.org/10.1175/2009MWR2850.1>

Kuo, H.-C., Chang, C.-P. & Liu, C.-H. (2012). Convection and rapid filamentation in Typhoon Sinlaku during TCS-08/T-PARC. *Monthly Weather Review*, 140, 2806-2817. <https://doi.org/10.1175/MWR-D-11-00314.1>

Kuo, H.-C., Tsujino, S. Huang, C.-C., Wang, C.-C., & Tsuboki, K. (2019). Diagnosis of the dynamic efficiency of latent heat release and the rapid intensification of Supertyphoon Haiyan (2013). *Monthly Weather Review*, 147, 1127-1147. <https://doi.org/10.1175/MWR-D-18-0149.1>

Kuo, H.-C., Tsujino, S., Hsu, T.-Y., Peng, M. S., & Su, S.-H. (2022) Scaling law for boundary layer inner eyewall pumping in concentric eyewalls. *Journal of Geophysical Research: Atmospheres*, 127, e2021JD035518. <https://doi.org/10.1029/2021JD035518>



Ladwig, W., (2017). wrf-python (version 1.3.4.1) [software]. Boulder, Colorado:

UCAR/NCAR. <https://doi.org/10.5065/D6W094P1>

Lai, T.-K., E. A. Hendricks, K. Menelaou, & M. K. Yau (2021). Roles of Barotropic

Instability across the Moat in Inner Eyewall Decay and Outer Eyewall

Intensification: Three-Dimensional Numerical Experiments. *Journal of the*

Atmospheric Sciences, 78, 473-496. <https://doi.org/10.1175/JAS-D-20-0168.1>

Lim, K.-S. S., & Hong, S.-Y. (2010). Development of an effective double-moment cloud

microphysics scheme with prognostic cloud condensation nuclei (CCN) for weather

and climate models. *Monthly Weather Review*, 138, 1587-1612.

<https://doi.org/10.1175/2009MWR2968.1>

Marks, F. D., Black, P. G., Montgomery, M. T., & Burpee, R. W. (2008). Structure of the

Eye and Eyewall of Hurricane Hugo (1989). *Monthly Weather Review*, 136(4),

1237-1259. <https://doi.org/10.1175/2007MWR2073.1>

Miyamoto, Y., & Takemi, T. (2013). A transition mechanism for the spontaneous

axisymmetric intensification of tropical cyclones. *Journal of the Atmospheric*

Sciences, 70, 112-129. <https://doi.org/10.1175/JAS-D-11-0285.1>

Mlawer, E. J., Taubman, S. J., Brown, P. D., Iacono, M. J., & Clough, S. A. (1997).

Radiative transfer for inhomogeneous atmospheres: RRTM, a validated correlated-

k model for the longwave. *Journal of Geophysical Research: Atmospheres.*, 102,



16663-16682. <https://doi.org/10.1029/97JD00237>

Qin, N., Wu, L., & Liu, Q. (2021). Evolution of the Moat Associated with the Secondary Eyewall Formation in a Simulated Tropical Cyclone. *Journal of the Atmospheric Sciences*, 78, 4021-4035. <https://doi.org/10.1175/JAS-D-20-0375.1>

Rogers, R., & Reasor, P. (2013). Airborne Doppler Observations of the Inner-Core Structural Differences between Intensifying and Steady-State Tropical Cyclones. *Monthly Weather Review*, 141, 2970-2991. <https://doi.org/10.1175/MWR-D-12-00357.1>

Rozoff, C. M., Schubert, W. H., McNoldy, B. D., & Kossin, J. P. (2006). Rapid filamentation zones in intense tropical cyclones. *Journal of the Atmospheric Sciences*, 63, 325-340. <https://doi.org/10.1175/JAS3595.1>

Sawyer, J. S. (1956) The Vertical Circulation at Meteorological Fronts and Its Relation to Frontogenesis. *Proceedings of the Royal Society A*, 234, 346-362. <https://doi.org/10.1098/rspa.1956.0039>

Skamarock, W. C., Klemp, J. B., Dudhia, J., Gill, D. O., Barker, D. M., Wang, W., & Powers, J. G. (2008). A description of the Advanced Research WRF version 3. *NCAR Tech Note NCAR/TN-4751STR*, 113. <https://doi.org/10.5065/D68S4MVH>.

Tsujino, S., Tsuboki, K., & Kuo, H.-C. (2017). Structure and maintenance mechanism of long-lived concentric eyewalls associated with simulated Typhoon



Bolaven (2012). *Journal of the Atmospheric Sciences*, 74, 3609-3634.

<https://doi.org/10.1175/JAS-D-16-0236.1>

Wang, H., Wu, C.-C., & Wang, Y. (2016). Secondary Eyewall Formation in an Idealized

Tropical Cyclone Simulation: Balanced and Unbalanced Dynamics. *Journal of the*

Atmospheric Sciences, 73(10), 3911-3930. <https://doi.org/10.1175/JAS-D-15->

[0146.1](https://doi.org/10.1175/JAS-D-15-0146.1)

Wang, Y.-F., & Tan, Z.-M. (2020). Outer rainbands–driven secondary eyewall formation

of tropical cyclones. *Journal of the Atmospheric Sciences*, 77, 2217-2236.

<https://doi.org/10.1175/JAS-D-19-0304.1>

Willoughby, H. E., Clos, J. A., & Shoreibah, M. G. (1982). Concentric Eye Walls,

Secondary Wind Maxima, and the Evolution of the Hurricane Vortex. *Journal of*

the Atmospheric Sciences, 39, 395-411. <https://doi.org/10.1175/1520->

[0469\(1982\)039%3C0395:CEWSWM%3E2.0.CO;2](https://doi.org/10.1175/1520-0469(1982)039%3C0395:CEWSWM%3E2.0.CO;2)

Yang, Y.-T., Kuo, H.-C. Hendricks, E. A., & Peng, M. S. (2013). Structural and intensity

changes of concentric eyewall typhoons in the western North Pacific basin. *Monthly*

Weather Review, 141, 2632-2648. <https://doi.org/10.1175/MWR-D-12-00251.1>

Yang, Y. T., Kuo, H. C., Tsujino, S. Chen, B. F., & Peng, M. S. (2021). Characteristics of

the Long-Lived Concentric Eyewalls in Tropical Cyclones. *Journal of Geophysical*

Research: Atmospheres, 126, e2020JD033703.

<https://doi.org/10.1029/2020JD033703>



Tables



Table 1. Ranges of Forcing Terms for the Sawyer-Eliassen Equation in Each Diagnosis.

Q is the diabatic heating rate including latent heating, and **F** is the momentum forcing term from PBL Scheme.

| Diagnosis experiment | Range of Q | Range of F |
|----------------------|--------------------------------|--------------------------------|
| Diag1 | entire diagnosed domain | entire diagnosed domain |
| Diag2 | inside the concentric eyewalls | no |
| Diag3 | no | inside the concentric eyewalls |
| Diag4 | inner eyewall | no |
| Diag5 | moat | no |
| Diag6 | outer eyewall | no |
| Diag7 | no | inner eyewall |
| Diag8 | no | moat |
| Diag9 | no | outer eyewall |

Figures

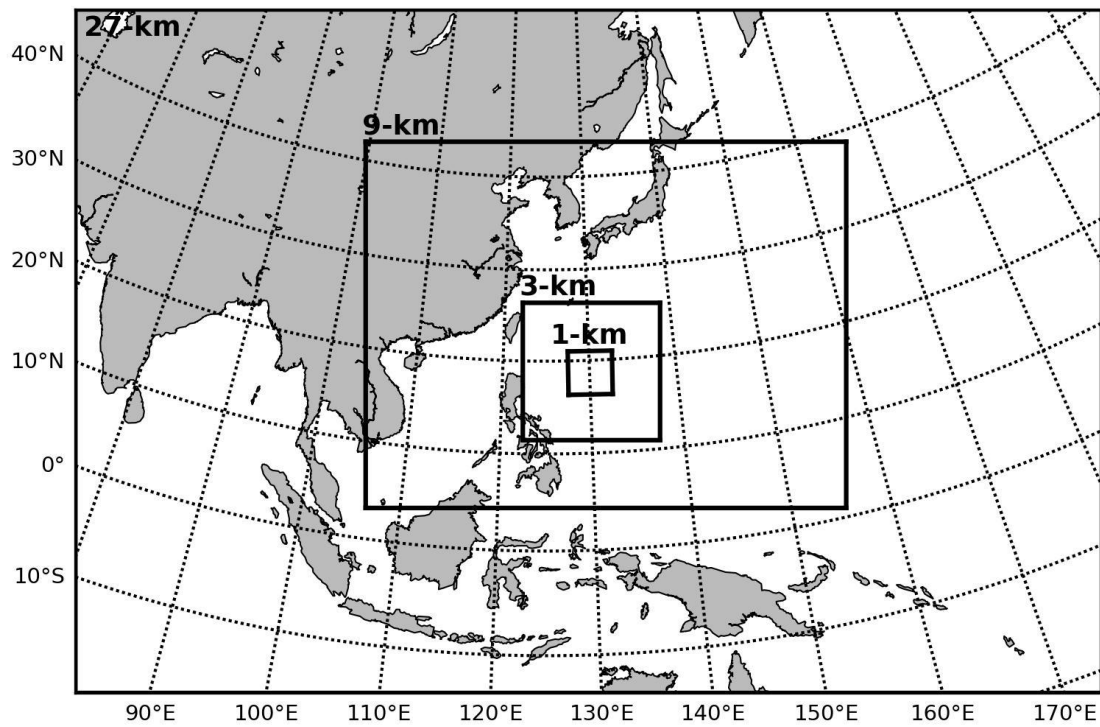
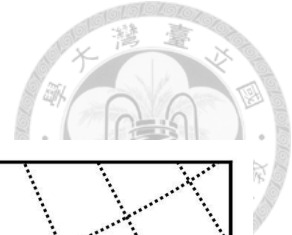


Figure 1: The nested domain of the WRF model and the track of TC Lekima from 0000 UTC 5 August to 11 August 2019. Note that both the 3-km and 1-km domains are moving with the TC, with the center of the 1-km domain located at the eye of TC Lekima.

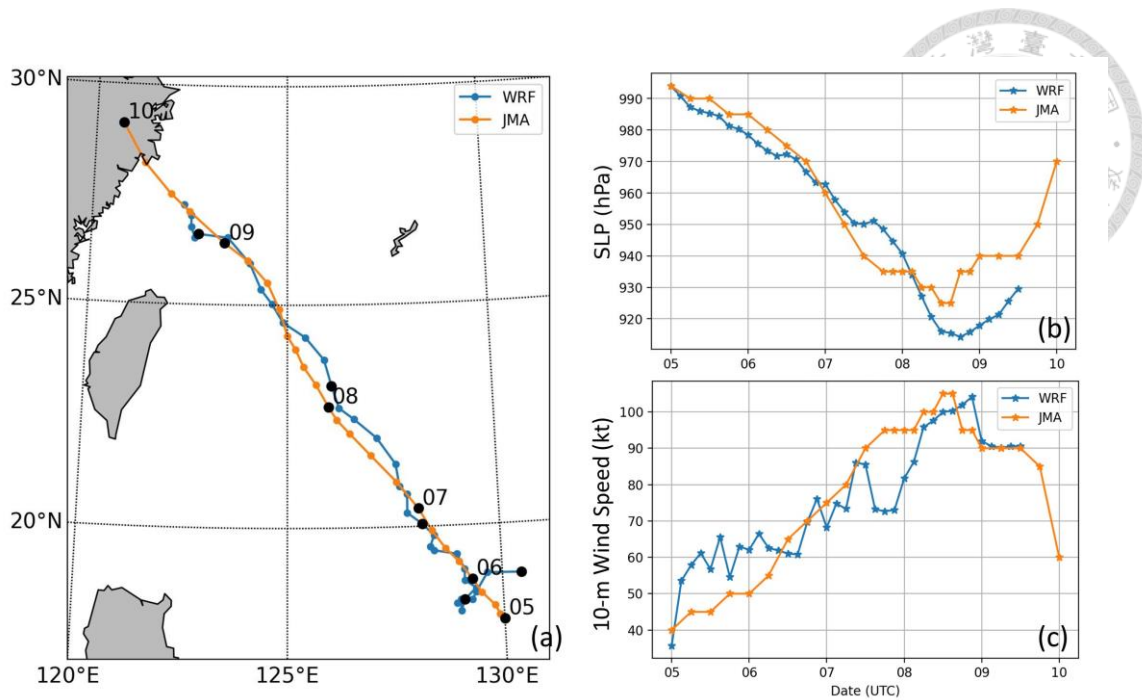


Figure 2: The (a) tracks, (b) sea-level pressure (hPa), and (c) 10-m height wind speed (kt) of TC Lekima from the JMA best-track data (in orange) and the WRF simulation (in blue). The dots are marked every 6 hours. The black dots marked with numbers along the track in (a) indicate the positions of TC Lekima at 0000 UTC that day.

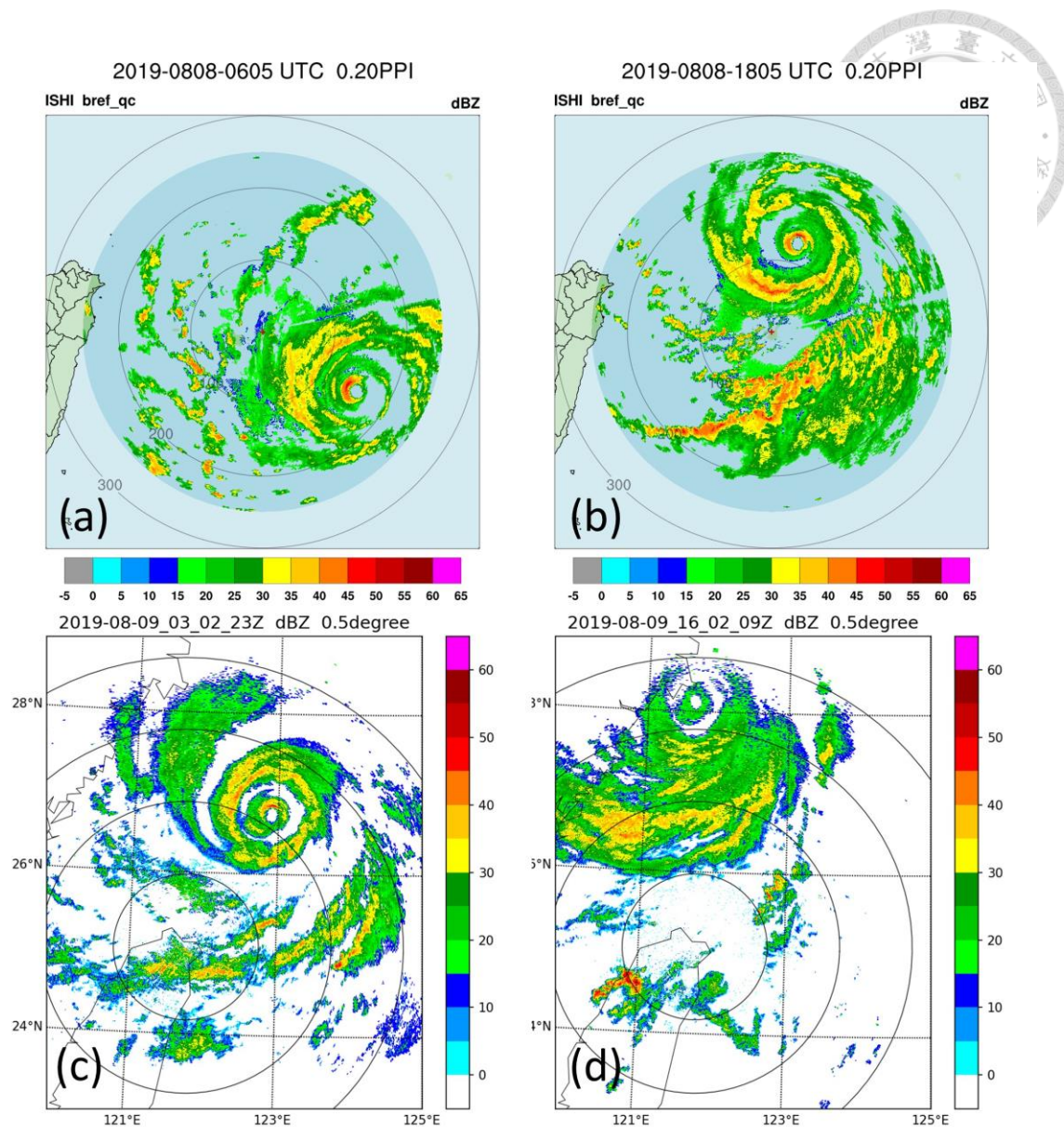


Figure 3: The 0.2° elevation angle PPI reflectivity (colored; dBZ) from the radar on Ishigaki Island at (a) 0605 UTC and (b) 1805 UTC 8 August 2019, and the 0.5° elevation angle PPI reflectivity (dBZ) from the radar on Wufen Mountain at (c) 0302 UTC and (d) 1602 UTC on 9 August 2019.

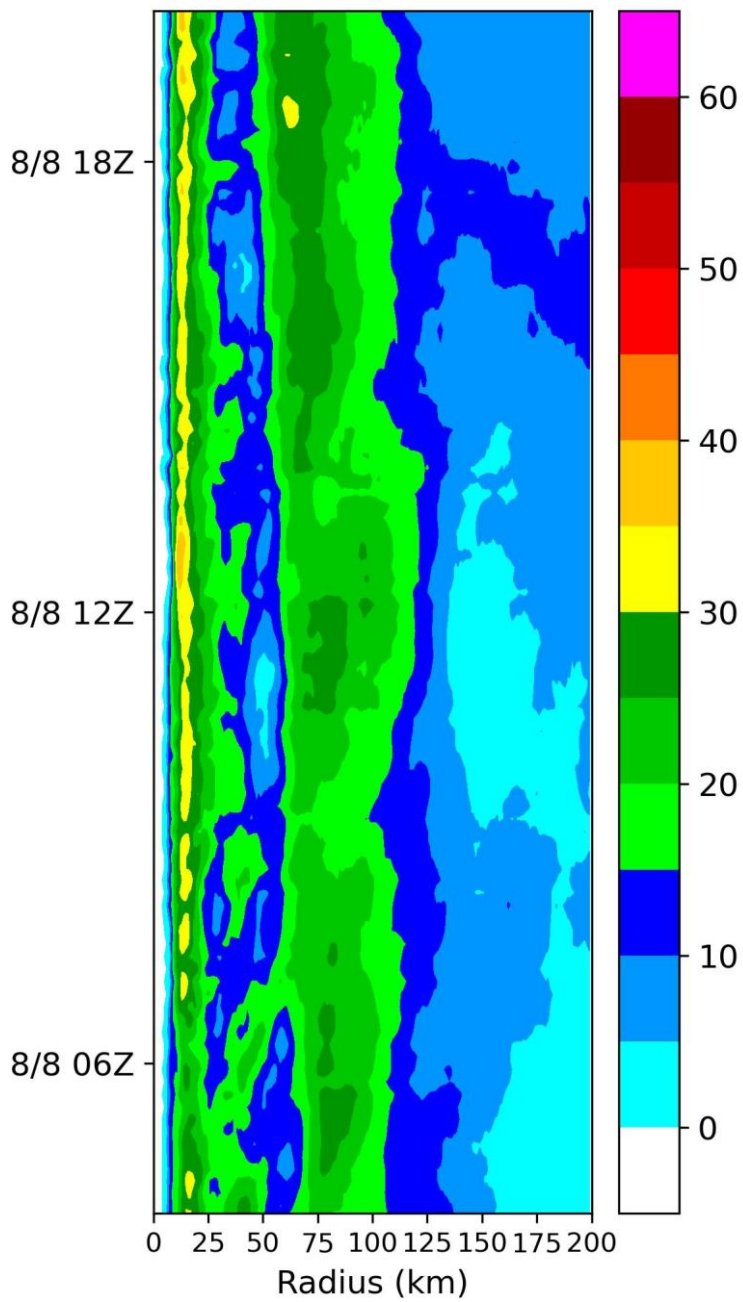


Figure 4: Hovmöller diagram of 2-km azimuthally-averaged reflectivity (colored: dBZ)

observed by Ishigaki Island radar.

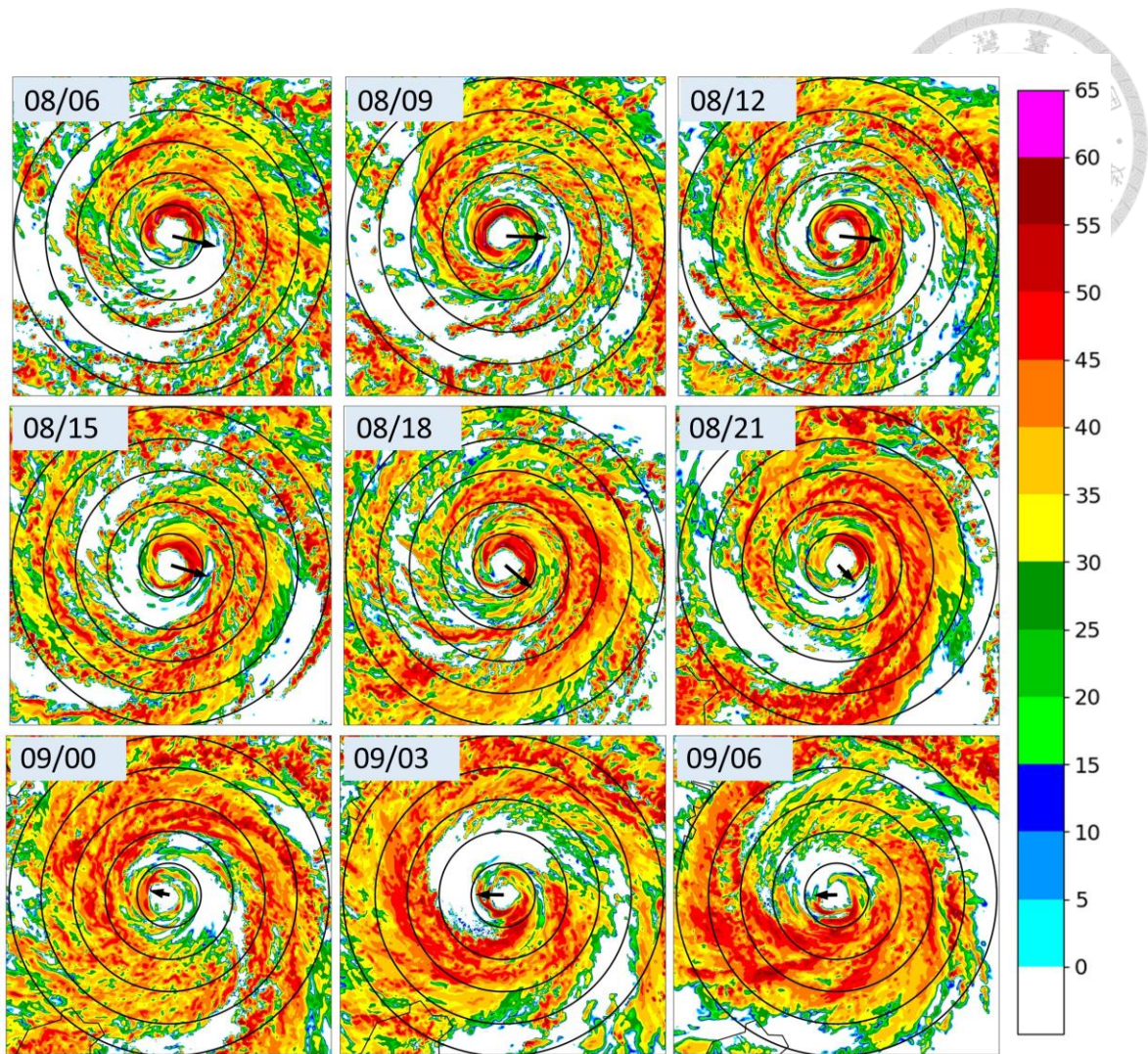


Figure 5: Simulated reflectivity (colored; dBZ) at the height of 2 km from 06 UTC on 8 August 2019 to 06 UTC on 9 August 2019 with an interval of 3 hours. The black circles indicate the distances from the TC center with an interval of 40 km. The arrow indicated the vertical wind shear direction between 200 and 850 hPa averaged from $r = 200$ km to $r = 800$ km. Numbers on the upper left of each panel indicate the date and hour (UTC).

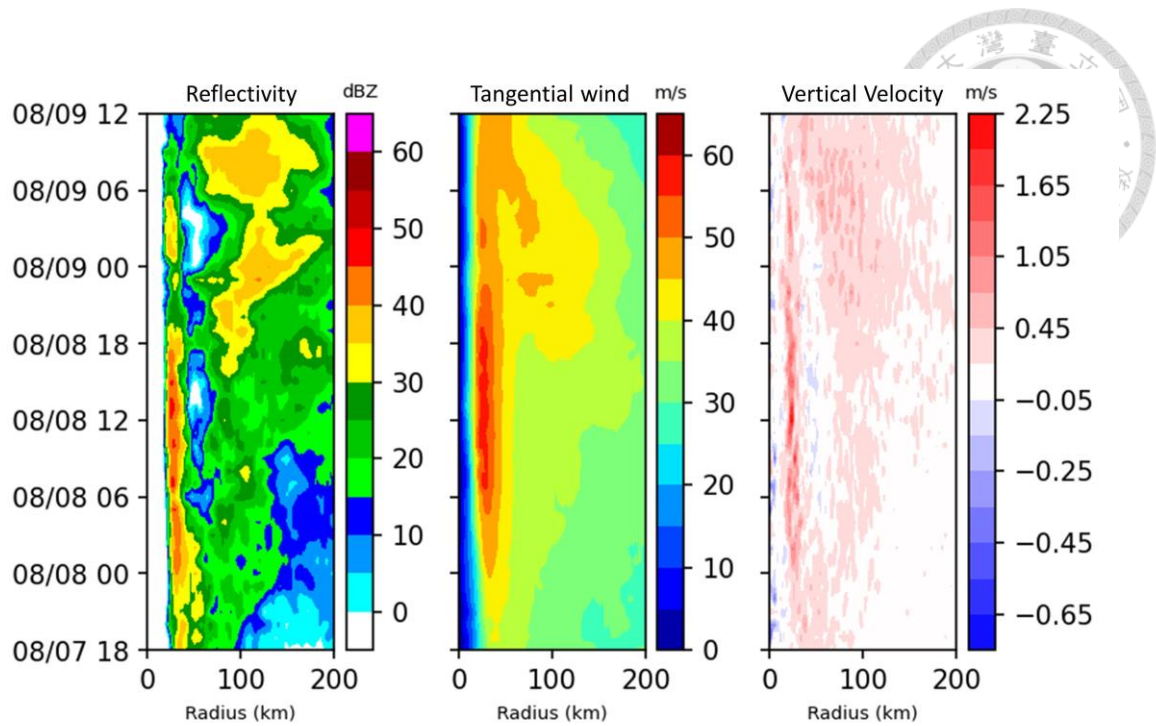


Figure 6: Hovmöller diagram of the simulated azimuthally-averaged (a) reflectivity (colored; dBZ), (b) tangential wind (colored; m s^{-1}), and (c) vertical velocity (colored; m s^{-1}) at $z = 2$ km. Note that the color scale for negative vertical velocity in (c) is smaller to clarify the moat downdraft.

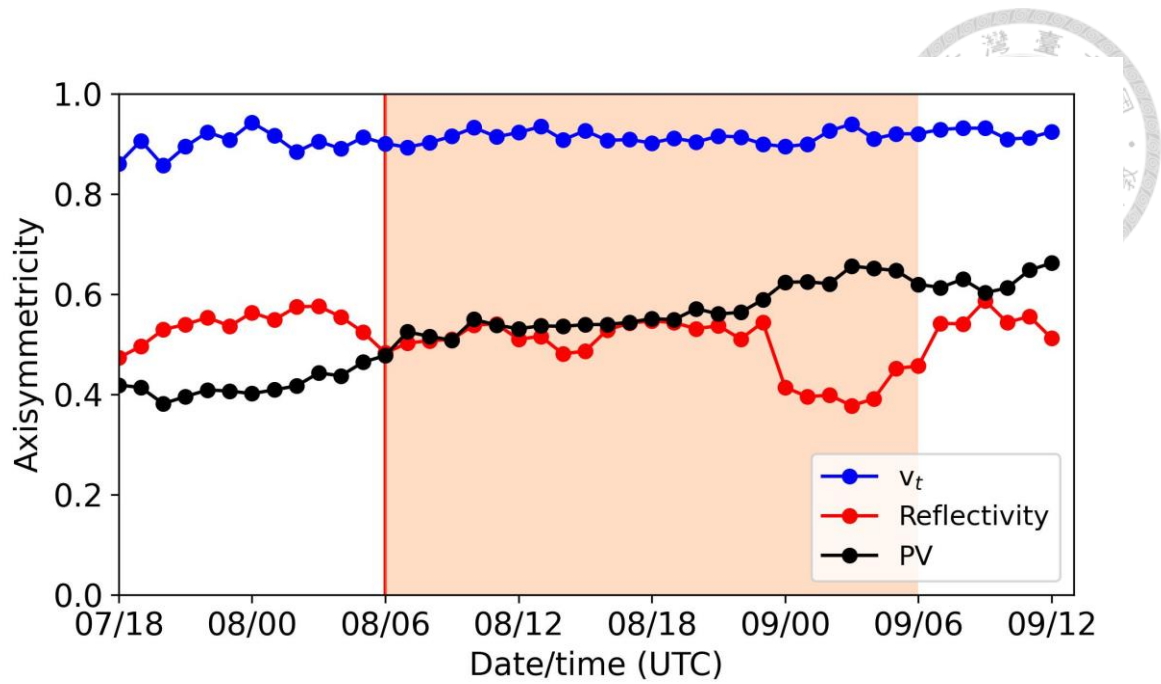


Figure 7: Axisymmetry parameter of tangential wind (blue), reflectivity (red), and potential vorticity (black) from 7 to 9 August 2019. The orange shading indicates the diagnosed period. The red line indicates the secondary eyewall formation time.

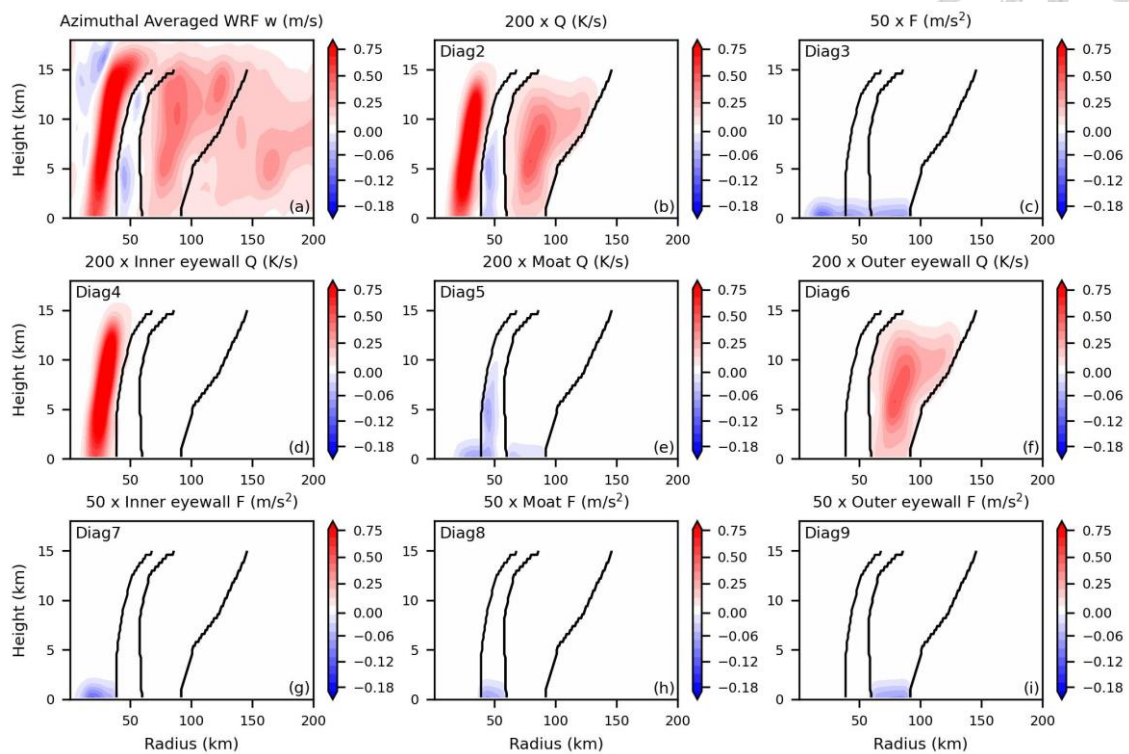


Figure 8: (a) Azimuthally-averaged simulated vertical velocity (colored; m s^{-1}); (b), (d), (e), and (f) the corresponding latent heating (colored; K s^{-1}) in Diag2, Diag4, Diag5, Diag6, respectively; and (c), (g), (h), (i) the corresponding momentum forcing (colored; m s^{-2}) term in Diag3, Diag7, Diag8, and Diag9, respectively, at 1300 UTC on 8 August 2019. The black lines indicate the outer boundary of the inner eyewall, inner boundary of the outer eyewall, and outer boundary of the outer eyewall. Note that the color scale for negative values is smaller to clarify the moat downdraft and latent cooling rate. Text at the upper-left corner in (b) to (i) indicates the diagnosis experiment.

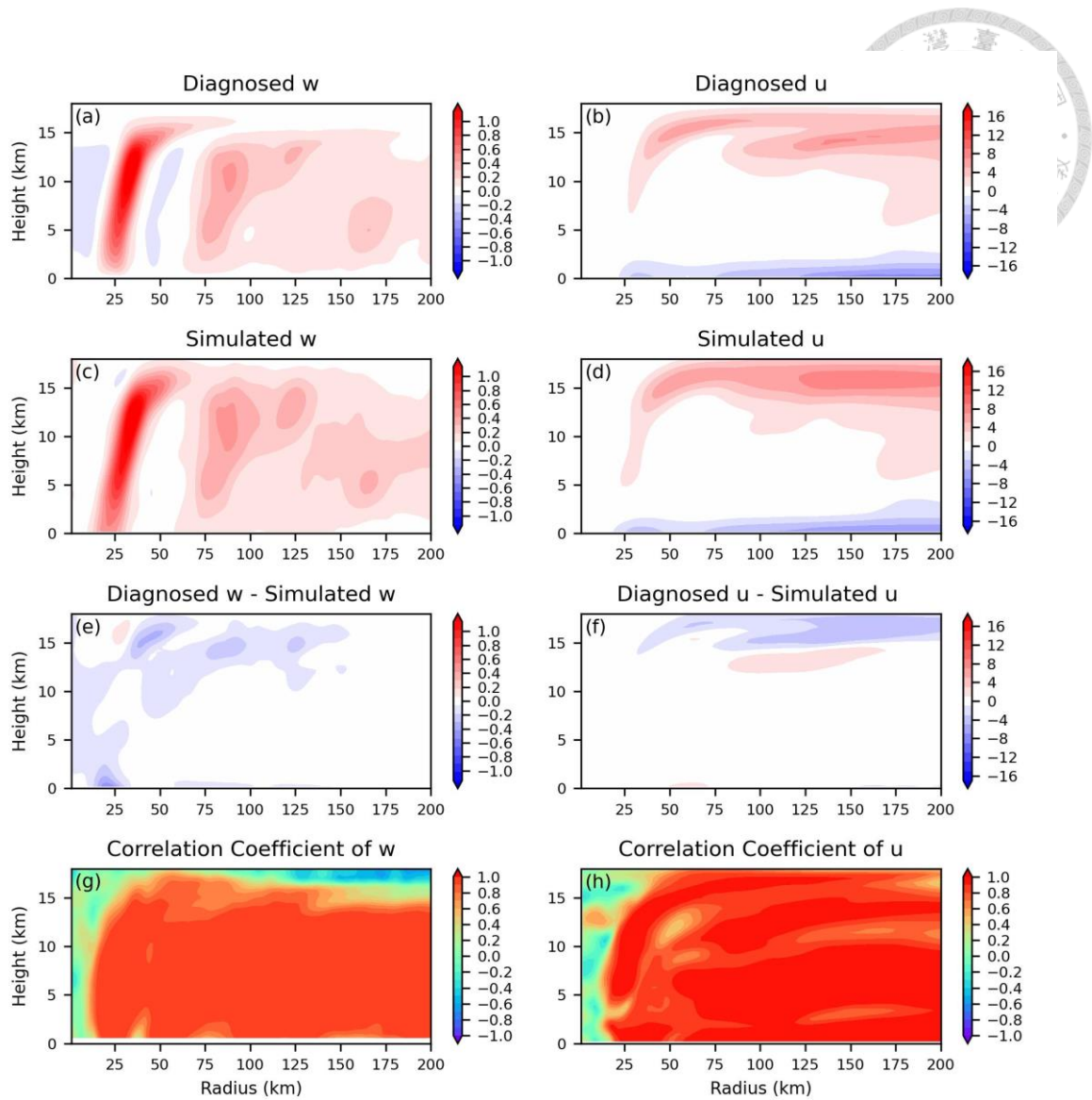


Figure 9: Diagnosed (a) vertical velocity (colored; m s^{-1}) and (b) radial wind (colored; m s^{-1}) by the Sawyer-Eliassen equation. Azimuthally-averaged (c) vertical velocity and (d) radial wind by the WRF simulation. Difference between diagnosed and simulated (e) vertical velocity and (f) radial wind (diagnoses – simulated). Correlation coefficients of (g) vertical velocity and (h) radial wind between the diagnosis and the simulation. Results are at 1300 UTC on 8 August 2019.

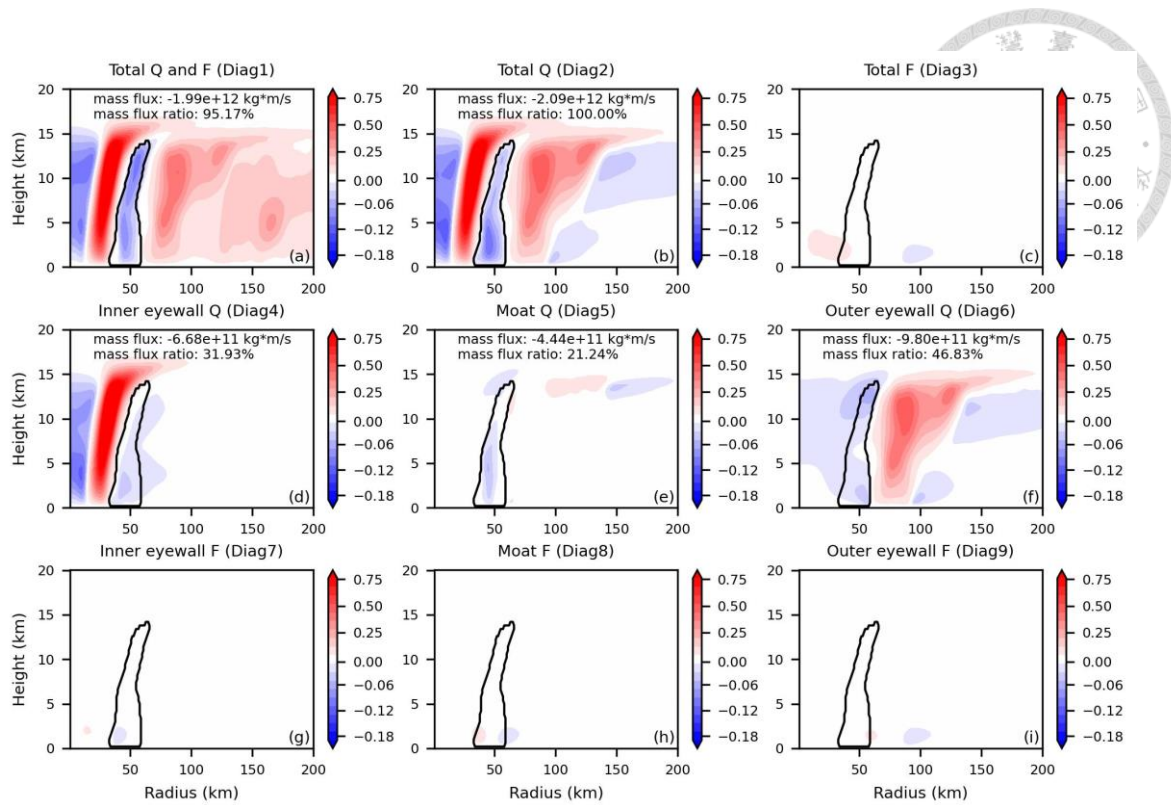


Figure 10: Diagnosed vertical velocity (colored; m s^{-1}) by considering (a) the latent heating and momentum forcing in the entire domain at 1300 UTC on 8 August 2019. (b-i) Diagnosed vertical velocity by considering the corresponding forcing terms in Figs. 8b to 8i. The black lines in each panel indicate the range of moat downdraft in (b). Text at the upper side of the panel (a), (b), and (d)-(f) indicates the mass flux of the moat downdraft and the mass flux ratio to that in (b). The color scale for negative values is smaller to clarify the moat downdraft and latent cooling rate.

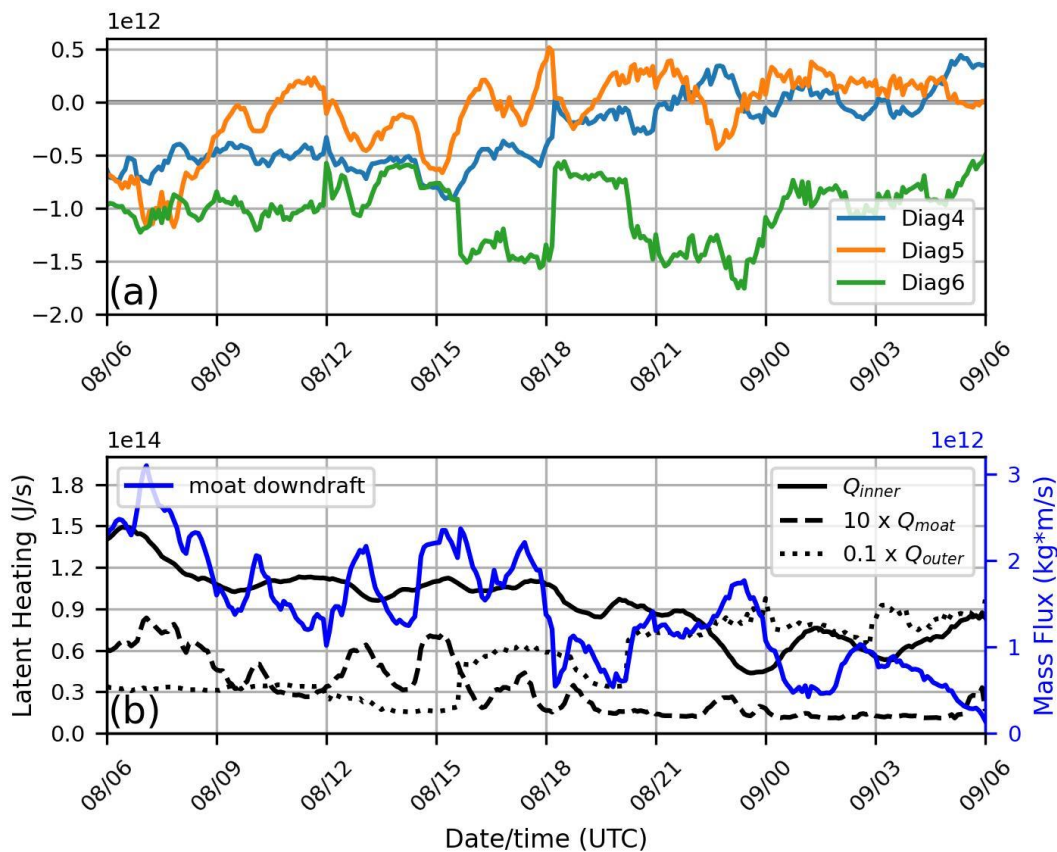


Figure 11: (a) Time series of mass flux of the diagnosed moat downdraft in Diag4 (blue line; kg m s^{-1}), Diag5 (orange line; kg m s^{-1}), and Diag6 (green line; kg m s^{-1}) from 0600 UTC 8 August 2019 to 0600 UTC 9 August 2019 with the 5-min interval. (b) Time series of latent heating in the inner eyewall (solid black line; J s^{-1}), 10 times of latent cooling in the moat (dashed black line; J s^{-1}), 0.1 times of latent heating in the outer eyewall (dotted black line; J s^{-1}), and the simulated moat downdraft mass flux (blue line; kg m s^{-1}).

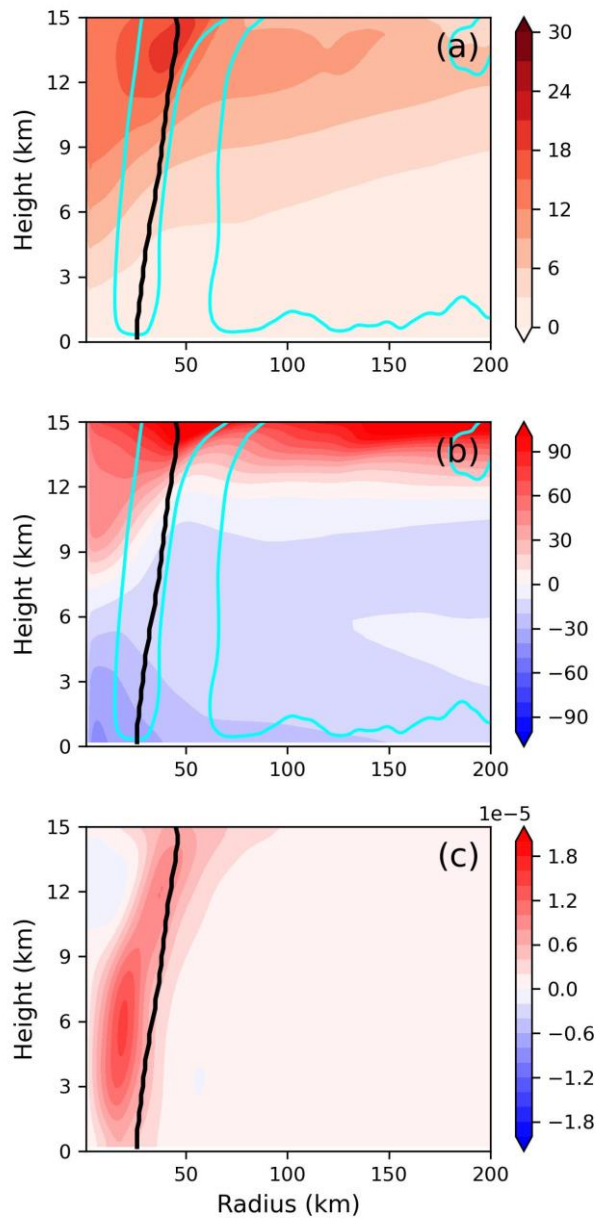


Figure 12: (a) Diagnosed DEF of latent heating (colored; %), (b) diagnosed DEF of momentum (colored; %), (c) simulated azimuthal-averaged baroclinicity (colored; s^{-2}) at 1300 UTC 8 August 2019. The black lines indicate the locations of the radius of maximum wind (RMW) at each altitude, and the cyan lines in (a) and (b) indicate the azimuthally-averaged vertical velocity of 0.05 ms^{-1} .

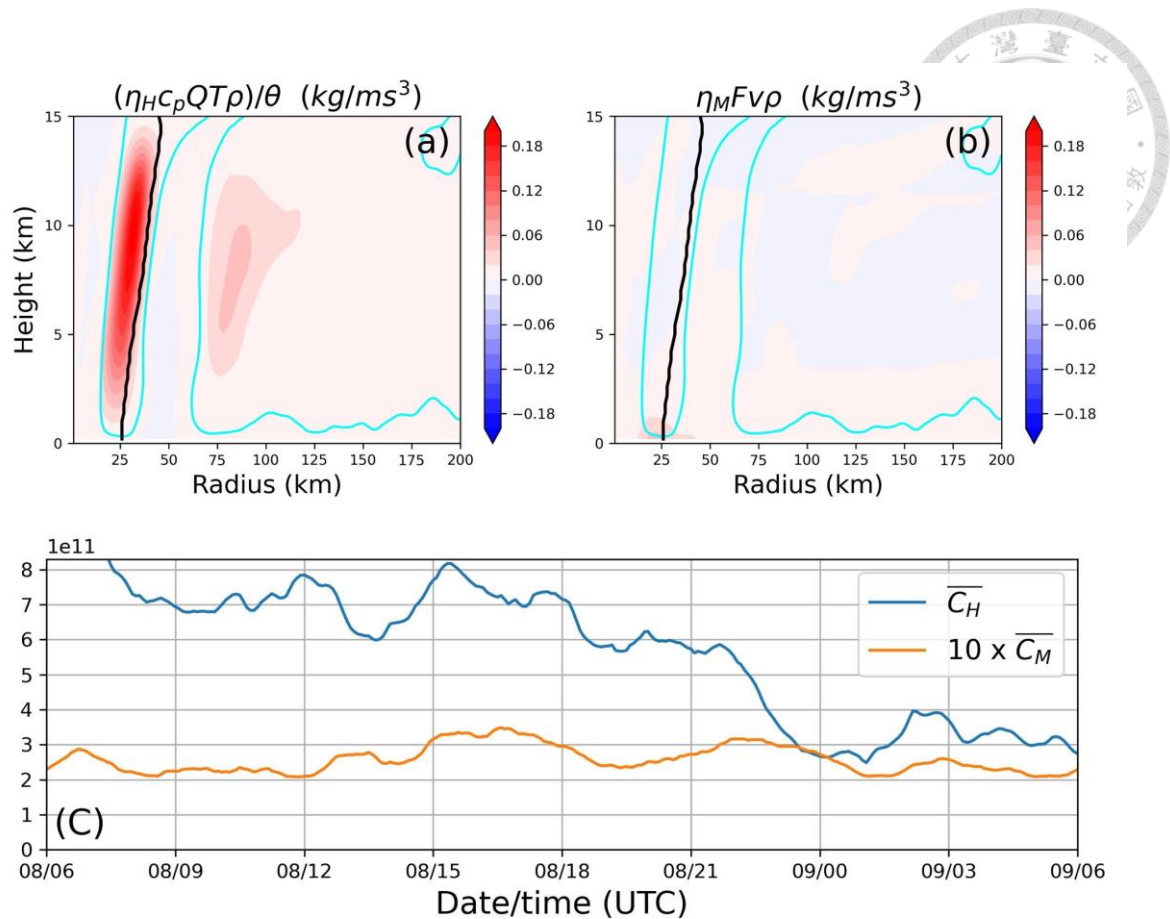


Figure 13: (a) Conversion rate by latent heating at each grid point (colored; $\text{kg m}^{-1} \text{s}^{-3}$) and (b) conversion rate by momentum forcing at each point (colored; $\text{kg m}^{-1} \text{s}^{-3}$) at 1300 UTC on 8 August 2019. (c) conversion rate by latent heating ($\overline{C_H}$; blue line; $\text{kg m}^2 \text{s}^{-2}$) and 10 times conversion rate by momentum forcing ($\overline{C_M}$; blue line; $\text{kg m}^2 \text{s}^{-2}$) from 1100 UTC to 1700 UTC on 8 August 2019 inside $r = 40$ km. Cyan and black lines in (a) and (b) indicate the azimuthally-averaged vertical velocity of 0.05 m s^{-1} and the radius of maximum wind (RMW), respectively.

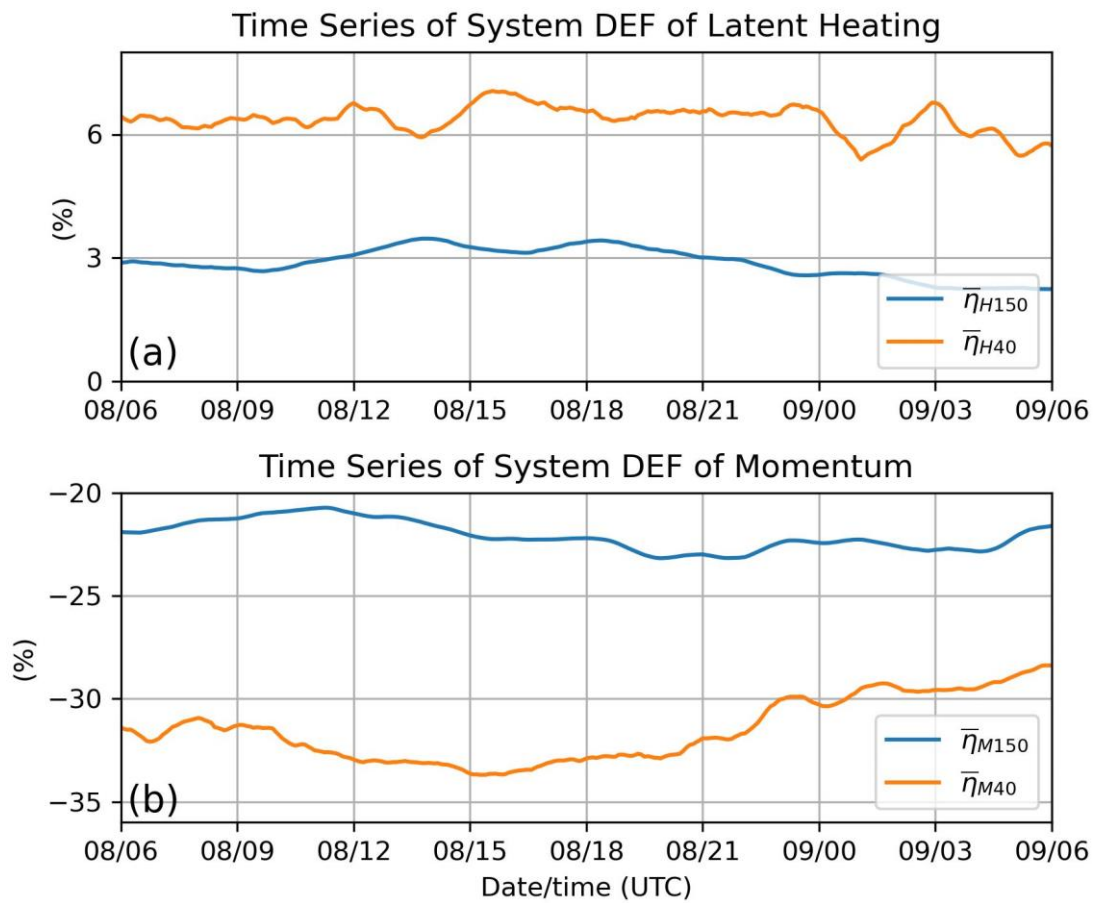


Figure 14: (a) Time series of system DEF of latent heating for $\bar{\eta}_{H40}$ (orange line; %) and $\bar{\eta}_{H150}$ (blue line; %) as well as (b) time series of system DEF of momentum for $\bar{\eta}_{M40}$ and $\bar{\eta}_{M150}$ from 1100 UTC to 1700 UTC on 8 August 2019.